



**POLITECNICO
DI MILANO**

SCUOLA DI INGEGNERIA INDUSTRIALE E DELL'INFORMAZIONE

DIPARTIMENTO DI ENERGIA

Master of Science in Energy Engineering

**Numerical Modelling of Convective Heat Losses of a Real
Scale Cavity Receiver Used in Solar Thermal Power Towers**

Supervisor: Professor Fabio Inzoli
Company Supervisor: Dr. Silvan Siegrist

Seyed Mohammad Kobari
Matricola: 815613
Student ID: 10446644

Academic Year 2016/2017

Abstract

Using cavity receivers in the solar thermal towers as a solution to reduce the radiation losses from receiver was always a point of interest in the CSP (concentrating solar power) researches. Although the radiative losses could be reduced significantly by cavity receivers, the convective heat losses remain as a crucial factor on the efficiency of the receiver and overall system. However, the influence of wind on these losses has not been studied sufficiently for large scale commercial cavity receivers. In the present study, the influence of wind with Reynolds numbers in the range of $Re = 2.82 \times 10^6 - 1.07 \times 10^7$ on a cavity receiver with inclination of $\phi = 60^\circ$ and a Grashof Number of $Gr = 1.85 \times 10^{13}$ has been investigated and analyzed numerically.

This study has tried to investigate convective heat losses from a real scale cavity receiver with the nominal thermal power of $75 MW_{th}$. Results of this study shows that the convective heat losses in this scale and inclination level is highly related to forced convection induced by wind and can significantly affects the efficiency of the receiver. The results show an almost linear relation between the convective heat losses and wind velocity.

Shrinkage of the stagnation zone has been observed with all wind velocities and stagnation zone become smaller with higher wind speeds. As the convective heat losses in the stagnation zone are very small, the shrinkage of the stable stagnation zone and consequently a bigger convective zone with lower temperature and natural and forced convective flows in it, has been recognized as the main reason for the increase of the convective heat losses from the cavity.

Key words: Concentrating solar power, Cavity receiver, OpenFOAM, CFD, Mixed convection, Heat transfer, Renewable energy sources

Sommario

Negli studi relativi ai concentratori solari, l'utilizzo di ricevitori a cavità per la produzione di energia tramite impianti a torre di energia solare è sempre risultato essere un tema rilevante al fine di ridurre la componente di irraggiamento delle perdite. Sebbene queste perdite possano essere ridotte significativamente tramite l'impiego di ricevitori a cavità, la componente convettiva rimane un fattore cruciale per l'efficienza del ricevitore e, di conseguenza, dell'intero sistema. Tuttavia, l'impatto dei fenomeni ventosi relativo a queste perdite per le tipologie di ricevitori presenti sul mercato non è stato oggetto di approfondite ricerche. In questo studio sono stati analizzati gli effetti del vento utilizzando numeri di Reynolds tra $Re = 2.82 \times 10^6 - 1.07 \times 10^7$ su un ricevitore con inclinazione pari a $\phi = 60^\circ$ rispetto all'orizzonte e numero di Grashof uguale a $Gr = 1.85 \times 10^{13}$.

Questa analisi ha avuto come obiettivo quello di studiare il comportamento delle perdite per convezione provenienti da un ricevitore a cavità di dimensioni reali avente una potenza nominale pari a $75 MW_{th}$. I risultati riportano che le perdite per convezione e l'inclinazione del ricevitore sono strettamente dipendenti dalla convezione forzata prodotta dal vento e possono incidere significativamente sull'efficienza del ricevitore. Inoltre, è stato dimostrato come la dipendenza tra le perdite convettive e la velocità del vento sia quasi lineare.

E' stato stimato che, all'aumentare della velocità del vento, la zona di stagnazione diminuisce. Poiché le perdite convettive nell'intorno della zona di stagnazione sono molto contenute, il restringimento della zona di stagnazione stabile, che comporta un aumento della zona convettiva del ricevitore caratterizzata da temperature minori ed un flusso a convezione sia naturale che forzata, è stato riconosciuto essere la causa principale dell'aumento di perdite per convezione dal ricevitore.

Parole chiave: Concentratori solari, Ricevitore a cavità, OpenFOAM, CFD, Convezione mista, Trasferimento di calore, Energie rinnovabili

Acknowledgements



**Deutsches Zentrum
für Luft- und Raumfahrt**
German Aerospace Center

This master thesis work has been carried out in German Aerospace Center (DLR), Jülich division, Germany in collaboration with RWTH Aachen University and has been financially supported by the Ministry of Innovation, Science and Research of the State of North Rhine-Westphalia (MIWF NRW), Germany under contract 3007642 (Start-SF).

I would like to thank all the members of the Solar Research Institute (Institut für Solarforschung) of DLR, for their support and collaboration during the 6 months of my research in their institute, specially, Dr. Silvan Siegrist, my dear supervisor at DLR who patiently and friendly helped me step by step along this way.

I would like to express my gratitude to Professor Fabio Inzoli, Director of the Energy Department and my dear supervisor at Politecnico di Milano who supported me and this project from the day one till the last, and helped me to overcome the administrative problems.

Last but not least, I would like to thank my beloved family and all fantastic friends in Iran, Italy and Germany for their support, and motivating me along this journey. With no doubt, finishing this journey was not possible without their amazing presence in my life.

TABLE OF CONTENTS

Abstract	1
Sommario	2
Acknowledgements.....	3
List of Figures	6
Abbreviations	8
1 Introduction	10
1.1 Overview	10
1.2 Solar tower power plants.....	10
1.3 Cavity receivers	11
1.3.1 Thermal losses in the receiver of a solar tower	11
1.3.2 Convection losses in the cavity	12
1.4 Receiver model.....	15
1.5 Wind properties	16
1.5.1 Wind velocity.....	16
1.5.2 Wind direction.....	16
2 Numerical method	17
2.1 Computational fluid dynamics (CFD).....	17
2.2 ICEM	19
2.3 OpenFOAM.....	20
2.4 Turbulence modelling	21
2.4.1 Standard $k - \epsilon$	22
2.4.2 Realizable $k - \epsilon$	23
2.4.3 Standard $k - \omega$	24
2.4.4 $k - \omega SST$	25
2.5 Dimensionless wall distance	27
3 Simulation setup	28
3.1 Geometry	28
3.2 Grid generation	29

3.2.1	Topology.....	29
3.2.2	Grid Quality	32
3.3	Simulation setup	36
3.3.1	Boundary type.....	36
3.3.2	Thermophysical properties	36
3.3.3	Turbulence Properties.....	37
3.3.4	RAS Properties.....	37
3.3.5	Initial Values	37
3.3.6	Boundary conditions	38
3.3.7	Solver.....	39
3.3.8	fvSolution	39
3.4	Determination of convective heat losses.....	40
4	Results and discussion.....	41
4.1	Wind effects on the cavity	41
4.1.1	$u = 5 \text{ m/s}$	43
4.1.2	$u = 9 \text{ m/s}$	45
4.1.3	$u = 15 \text{ m/s}$	47
4.1.4	$u = 19 \text{ m/s}$	49
4.2	Convective Losses from the receiver	51
4.3	Influence on the efficiency of the receiver	54
4.4	Convergence and Mesh sensitivity analysis.....	55
5	Conclusion and outlook.....	57
	Literature.....	59

LIST OF FIGURES

Figure 1-1 Schematic of a Solar Tower Power Plant.....	11
Figure 1-2 Different heat loss mechanisms from Cavity	12
Figure 1-3 Stagnation and Convective zones in the cavity by only considering natural convection.....	13
Figure 1-4 Temperature distribution in the cavity by only considering natural convection ...	14
Figure 1-5 Cavity Geometry [12].....	15
Figure 2-1 A schematic of Finite Difference Method [24].....	18
Figure 2-2 A schematic of Finite Element Method [24].....	18
Figure 2-3 A schematic of Finite Volume Method [24]	19
Figure 2-4 The overall process in ICEM	20
Figure 3-1 Cavity and Wind tunnel geometry, created in ANSYS workbench.....	28
Figure 3-2 Wind tunnel dimensions	29
Figure 3-3 Wind tunnel and cavity model in ANSYS ICEM.....	30
Figure 3-4 Blocking structure - side view.....	30
Figure 3-5 Blocking structure - 3D.....	31
Figure 3-6 O-Grid inside the cavity	31
Figure 3-7 Coarse Mesh(M6)	33
Figure 3-8 Medium mesh (M5)	34
Figure 3-9 Medium mesh (M4)	35
Figure 4-1 Temperature report line	42
Figure 4-2 Temperature distribution inside cavity (u = 0 m/s)	42
Figure 4-3 Natural convection flow out of Cavity (u = 0).....	43
Figure 4-4 Flow field around the cavity (u = 5 m/s).....	43
Figure 4-5 Flow field at the aperture (u = 5 m/s).....	44
Figure 4-6 Temperature distribution inside cavity (u = 5 m/s)	44
Figure 4-7 Temperature along TRL (u = 5 m/s)	45
Figure 4-8 Flow field around the cavity (u = 9 m/s).....	45
Figure 4-9 Flow field at the aperture (u = 9 m/s).....	46

Figure 4-10 Temperature distribution inside cavity (u = 9 m/s).....	46
Figure 4-11 Temperature along TRL (u = 9 m/s).....	47
Figure 4-12 Flow field around the cavity (u = 15 m/s).....	47
Figure 4-13 Flow field at the aperture (u = 15 m/s).....	48
Figure 4-14 Temperature distribution inside cavity (u = 15 m/s).....	48
Figure 4-15 Temperature along TRL (u = 15 m/s).....	49
Figure 4-16 Flow field around the cavity (u = 19 m/s).....	49
Figure 4-17 Flow field at the aperture (u = 19 m/s).....	50
Figure 4-18 Temperature distribution inside cavity (u = 19 m/s).....	50
Figure 4-19 Temperature along TRL (u = 19 m/s).....	51
Figure 4-20 Temperature comparison inside cavity with different wind velocities.....	52
Figure 4-21 Convective losses from Cavity.....	53
Figure 4-22 Heat losses from cavity walls in all meshes.....	53
Figure 4-23 Nusselt Number report in different cases.....	54
Figure 4-24 Percentage of Convective heat losses.....	54
Figure 4-25 Convergence history M4 (u = 5 m/s).....	55
Figure 4-26 Mesh sensitivity on u = 5 m/s.....	56
Figure 4-27 Mesh sensitivity on u = 15 m/s.....	56

ABBREVIATIONS

<i>CFD</i>	Computational fluid dynamics
<i>CSP</i>	Concentrated solar power
<i>d</i>	Inner diameter of cavity
<i>d_{ap}</i>	Aperture diameter
<i>Gr</i>	Grashof number
<i>RANS</i>	Reynolds averaged Navier-Stokes
<i>RAS</i>	Reynolds averaged simulation
<i>Re</i>	Reynolds number
<i>ref</i>	Reference
<i>Ri</i>	Richardson number
<i>TRL</i>	Temperature report line
π	Pi number
<i>g</i>	Gravitational acceleration
β	Volumetric expansion coefficient
<i>L_{cav}</i>	Length of Cavity
<i>l</i>	Length of Cavity
$^{\circ}\text{C}$	Celsius degree
<i>m</i>	Meter
ν	Kinematic viscosity
μ	Dynamic viscosity
ρ	Density
<i>s</i>	Second
<i>t</i>	time
<i>T</i>	Temperature
<i>T_{film}</i>	Film temperature
<i>T_{ref}</i>	Reference temperature
<i>T_w</i>	Wall temperature
<i>T_∞</i>	Ambient temperature
<i>u</i>	Velocity
<i>u_*</i>	Friction velocity
<i>U</i>	Velocity field in OpenFOAM
α	Empirically derived coefficient for stability of atmosphere
<i>K</i>	Kelvin
<i>A_s</i>	Sutherland coefficient
<i>T_s</i>	Sutherland temperature
<i>p</i>	Pressure

R	Gas constant
λ	Conductivity of fluid
k	Turbulence kinetic energy
ω	Specific rate of dissipation
SST	Shear stress transport
P_{rgh}	Dynamic pressure
U	Overall heat transfer coefficient
A	Area
st	Stagnation zone
Q	Heat transfer energy
Nu	Nusselt number

1 INTRODUCTION

1.1 Overview

Concentrated solar power or CSP as a way to exploit the solar energy has been always under attention in the past four decades and it has increased especially in the past decade. In CSP technologies only the direct solar radiation can be concentrated, and this technology is mostly favorable in cloudless regions with strong radiation. The advantage of CSP systems over many other renewable power plants is the high full load hours of its operation which can be achieved through its combination with heat storage and it is suitable to compensate the fluctuations in the other renewable technologies such as PV and wind turbines. Apart from the power generation, we are dealing with high temperature heat in this technology and, so it can be used in other engineering processes such as fuel production or metal productions.

1.2 Solar tower power plants

Figure 1.1 shows an example structure of a solar tower power plant. The direct solar irradiations are concentrated by mirrors, called heliostats onto a receiver, which is mounted in or on a tower. In the Receiver the heat transfer fluid is heated, which will be used in a steam generation process for generation of steam required for the power cycle. By using a thermal storage, the hot heat transfer fluid can be stored and used later to generate steam. In addition to this scheme, there are other schemes like an open volumetric receiver which is using air in front of the receiver as the heat transfer fluid by sucking it through a prosperous heat exchange medium which is heated up by the solar irradiations. There are different heat storage mechanisms, one example is utilizing a ceramic packed bed storage which is used in the solar tower power plant in Jülich, Germany.

Regardless of the design of the solar tower power plant, receiver is one of the most important parts that has to be investigated properly because a large part of the losses in the

system is happening in the receiver. These losses as illustrated in figure 1-3, can be the followings:

- Radiation losses
- Convective losses
- Conduction losses

Due to the very high temperatures in the receiver, losses are dominated by radiation and convection, as the conduction losses can be kept relatively small by good insulation [2].

The purpose of this research is to evaluate the convective heat losses from a real scale cavity receiver based on realistic operation condition using a CFD model.

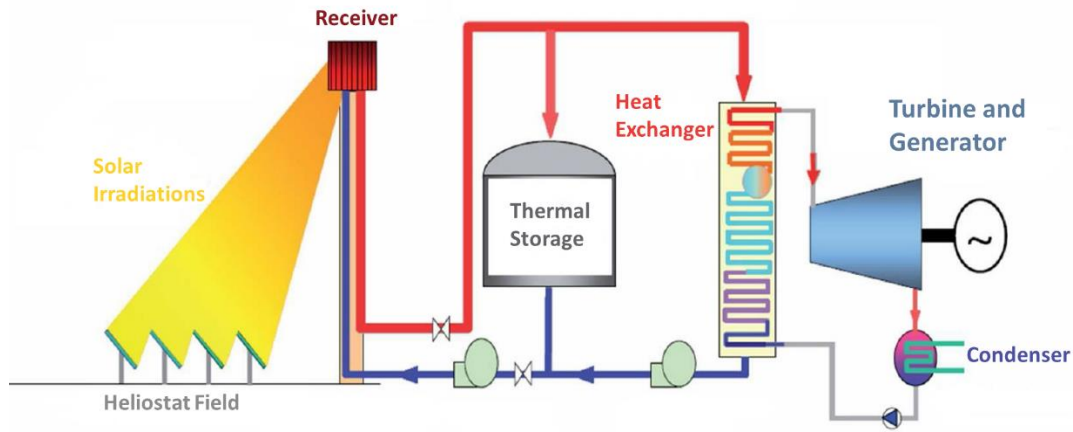


Figure 1-1 Schematic of a Solar Tower Power Plant

1.3 Cavity receivers

As we are dealing with temperatures in the order of 700 – 1000°C degree in the solar thermal towers, we can expect considerable thermal losses in the receiver. Controlling these thermal losses in the receiver is the key point on improving the performance of the overall system. To this matter, the idea of using a cavity for reducing the radiation losses came up in the past decades and it had a significant effect on controlling the radiative losses but still convective losses must be taken into consideration.

1.3.1 Thermal losses in the receiver of a solar tower

In the cavity receivers, the concentrated solar irradiations are passing through an opening in the cavity called aperture and the inner walls are absorbing the irradiations. As shown in figure 1-3, three major losses can exist in the receiver. Considering a well isolated cavity, the conductive heat losses through the cavity connections and the convective heat losses through

the outer surfaces of the cavity can be almost reduced to zero. The major losses remaining are the radiation and convective losses through the aperture. The calculation of the radiative losses is a complex phenomenon, but due to tools like ray tracing or even by analytical methods they can be estimated. The idea of using cavity receiver is to take benefit of the concept of a cavity to efficiently reduce the radiative losses. In technical designs radiative losses are eventually reduced to the same order of magnitude as the convective losses (McMordie, 1984 [1]; Kraabel, 1983 [3]).

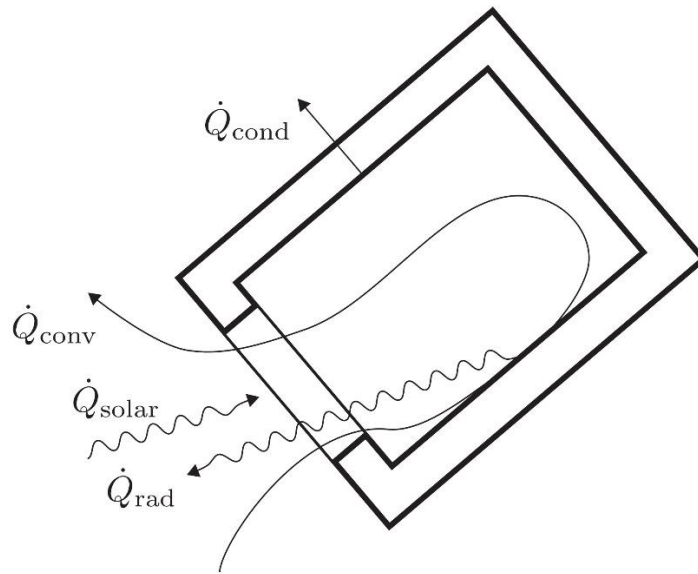


Figure 1-2 Different heat loss mechanisms from Cavity

1.3.2 Convection losses in the cavity

Convection is a highly nonlinear and complex problem, especially when external effects like wind are considered. As it is crucial to have an estimate for the convective losses, several studies dealt with an analysis of the convective losses of cavity receivers.

Basic mechanisms of the natural convection have been described by Eyer et al. (1979) [4] and Clausing et al. (1981) [5]. The hot air is trapped in the upper part of the cavity. The inner volume of the cavity can be divided into two zones as shown in Fig. 0-4 and Fig. 0-5 [5]. The upper part is the so-called stagnant zone. Here, the temperature is close to the wall temperature and the air is stably stratified. The lower part is the so-called convective zone. The cold air entering this zone through the aperture opening, is heated up and leaves the cavity through the upper part of the aperture. The boundary between the two zones can be approximated with the horizontal plane which goes through the upper lip of the aperture.

Since the receivers of interest are large, an experimental analysis requires a high effort. With increasing computational power nowadays, it is possible to analyze the convective losses with CFD simulations. Fang et al. [7] conducted a simulation of the influence of wind on an almost horizontal receiver. In the simulations wind increased the losses. The effect was

explained by an increased heat transfer coefficient due to higher velocities inside the cavity. Tan et al. [8] showed that wind can reduce the losses below the value of natural convection. The effect was used as a measure to reduce convective losses with an air curtain. Liovic et al. [9] performed experiments and simulations for a downwards facing cavity. The simulations were validated with data of thermocouples which were located outside of the receiver. The simulations showed that wind causes an increase of the convective losses. The influence of wind on cavity receivers with different inclination angles is analyzed numerically by Flesch et al. [12]. The effect of wind was found to depend strongly on the cavity orientation. For horizontal receivers wind had only a small influence whereas it had a huge impact on cavities with a high inclination angle.

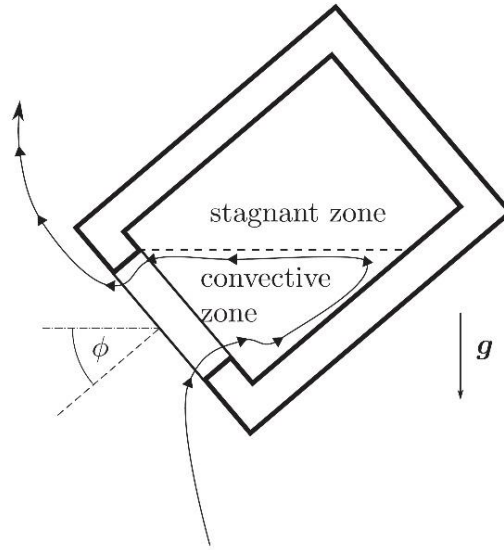


Figure 1-3 Stagnation and Convective zones in the cavity by only considering natural convection

Since the receivers designed for dishes are smaller and can be analyzed with lower effort, many studies on cavity receivers deal with the convective losses of cavities used in dish systems.

The Grashof number:

$$Gr = \frac{\beta_{ref}(T_{wall}-T_{\infty})gL_{cav}^3}{\nu_{ref}^2} \quad (1-1)$$

Where T_{ref} is the reference temperature and equal to film temperature

$$T_{ref} = T_{film} = 0.5 \times (T_{wall} + T_{\infty}) \quad (1-2)$$

In the Grashof number, β_{ref} denotes the volumetric expansion coefficient and $\nu_{ref} = \frac{\mu_{ref}}{\rho_{ref}}$ is the kinematic viscosity, both taken at the reference temperature and the ambient temperature and wall temperature are T_{∞} and T_{wall} respectively. The longest inner dimension (diameter or length) was taken as reference length L_{cav} . Since the dimension of the cavity receivers used in dish systems and solar towers are different, we are dealing with different

Grashof numbers and as a result dealing with different flow regimes caused by the natural convection phenomena in the cavity. Usually the cavity receivers that are used in the power towers, have a $Gr > 1.10^{10}$ [10]. Such a high value of Grashof number, means that we are dealing with turbulent flow inside the cavity due to the high buoyant forces.

Almost all the convective heat losses are happening in the convective zone, as both principal factors for a good convective heat transfer can be seen there, temperature difference and heat transfer coefficient due to the natural convection are both much higher than the stagnation zone.

The heat transfer coefficient and the border of the stagnation zone is not always the same and can be affected by the presence of wind in the aperture. In the literature and previous studies, there are contradictory results and statements on the effects of wind on the convective heat losses from the cavity. After some experiments on a solar tower cavity receiver, McMordie [1] concluded that wind does not have a significant effect on the convective heat losses of the cavity, while in the study carried out by Ma [11] on the cavity receiver for a parabolic concentrating solar collector, there is up to 3 times increase in the convective heat losses from the cavity. This contradiction has been explained by the fact that the receiver that was used in the experiment of McMordie almost had a vertical aperture and due to the slight changes of wind, changes in the ambient condition and high level of measurement error the effects may not have been recognized.

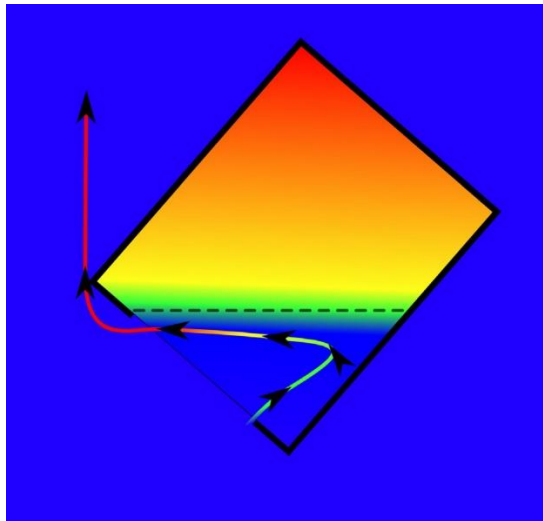


Figure 1-4 Temperature distribution in the cavity by only considering natural convection

A larger number of studies deal with the convective losses of cavities used in dish systems. The convective losses with and without wind were measured for a receiver with an inner diameter of 0.66 m by Stine and McDonald [13] and Ma [11]. Wind caused a significant increase of the losses. The losses of a small-scale receiver with an inner diameter of 0.07 m were measured by Taumoefolau et al. [14] without wind. This geometry was used in several subsequent studies, especially in order to validate CFD simulations. By performing a CFD

simulation, Paitoonsurikarn et al. [15] showed that CFD simulation can be used to predict the losses caused by natural convection for this geometry. Wu et al. [16] validated their CFD model with the experimental data as well and used their model to show that the losses can be reduced by decreasing the size of the aperture opening. In one experimental analysis by Wu et al. [17] the influence of a rotation on the heat loss of a receiver with the same geometry was found to be small. The numerical studies performed by Paitoonsurikarn et al. [18] and Xiao et al. [19] analyzed the influence of wind on this receiver. Both came to equivalent results: In the majority of the analyzed cases wind increased the convective losses. In some particular cases the losses with wind were lower than in case of natural convection. Prakash et al. [20] observed a similar effect while measuring the losses for a cavity receiver with an inner diameter of 0.33 m. An additional validation of CFD simulation was performed by Wu et al. [21] with a slightly enlarged version of the receiver from Taumoefolau et al. [14]. They used a constant heat flux boundary condition and included radiation in their model, but no wind. The CFD results were in good agreement with the experimental data. In a subsequent study the influence of wind on this receiver was analyzed experimentally [22]. Due to very low wall heat fluxes the wall temperature was below 100 °C in most of the cases. Wu et al. [22] observed a monotonically increasing Nusselt number with increasing wind speed.

1.4 Receiver model

The geometry of the cylindrical cavity that is used in this study is shown in figure 0-5. This geometry has been adopted from the study by Flesch et al. (2014) [12] and the size has been adjusted to the capacity of the intended solar power tower. A solar tower with the nominal Thermal Power of 75MW has been considered in this study. By considering an average flux of $200 \frac{kW}{m^2}$ on the tubes in the cavity and the overall thermal power of 75MW, the internal diameter of cavity can be calculated by solving the following equation:

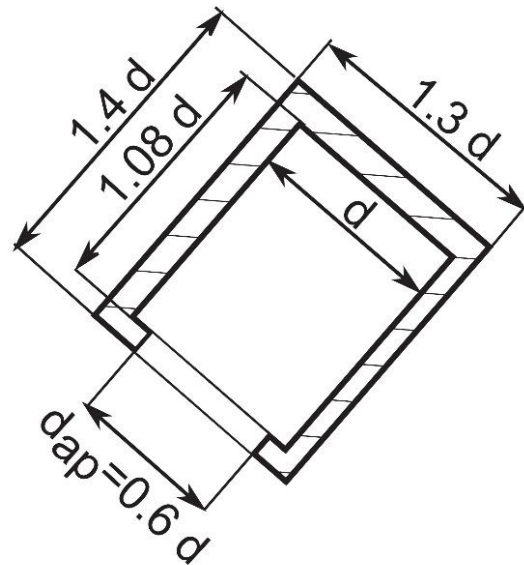


Figure 1-5 Cavity Geometry [12]

$$75 \text{ MW} = 200 \frac{\text{kW}}{\text{m}^2} \times \left[\frac{\pi d^2}{4} + \pi d(1.08d) \right] \quad (1-3)$$

And the result is:

$$d = 18.95 \text{ m}, \quad P_{ap} = 739 \frac{\text{kW}}{\text{m}^2} \quad (1-4)$$

1.5 Wind properties

1.5.1 Wind velocity

The main purpose of this study is to evaluate the convective losses of a real scale cavity in the presence of wind. Wind velocity is dependent to the geographical specification of each location and strongly to the altitude, so a general statement on wind speed is not possible and usually the frequency distribution of wind in each location can be identified by statistical data.

To find out the range of the wind speed that this study must consider, the maximum speed of the heliostats structures has been considered. According to Murphy et al [37], the wind speed limit for the structure of heliostats can be considered as $11 \frac{\text{m}}{\text{s}}$ at a height of 5 m . By assuming a solar power tower with the height of 200 m , the wind speed range can be calculated by equation (1-5),

$$\frac{u}{u_0} = \left(\frac{z}{z_0} \right)^\alpha \quad (1-5)$$

As mentioned before, $u_0 = 11 \frac{\text{m}}{\text{s}}$, $z_0 = 5 \text{ m}$ and $z = 200 \text{ m}$. α is an empirically derived coefficient that varies dependent upon the stability of the atmosphere and can be related to the vegetation type of the land around the particular location. As an example, for neutral stability conditions, α is approximately $1/7$ or 0.143 . In this case and by considering a low grass land, α is considered as 0.15 .

By considering all the assumptions, the maximum wind velocity (u) that the cavity has to work and calculated by equation (1-5) is $19 \frac{\text{m}}{\text{s}}$.

1.5.2 Wind direction

In this study and in the simulations, ϕ the angle of the cavity axis with the horizon was fixed at 60° and only the head on wind, parallel to the axisymmetric plane of the cavity receiver has been considered.

It is good to notice that fluid properties inside the cavity have been evaluated at the film temperature:

$$T_{film} = \frac{(T_\infty + T_w)}{2} \quad (1-6)$$

Where T_∞ is the air temperature equal to 283.15K and T_w is equal to 1083.15K .

2 NUMERICAL METHOD

2.1 Computational fluid dynamics (CFD)

Computational Fluid Dynamics (CFD) is the science of modeling fluid flows using numerical approximations. Fluid flows are governed by mass, momentum and energy balance principles, which are typically expressed in the form of partial differential equations of Navier-Stokes (the momentum term is described in equation (2-1)).

$$\rho \left(\frac{\partial u}{\partial t} + u \cdot \nabla u \right) = -\nabla p + \mu \nabla^2 u \quad (2-1)$$

where u is the flow velocity, p is the pressure, μ viscosity and ρ is the density [23].

However, turbulent flows are inherently unsteady and the normal form of Navier-Stokes equations does not consider the fact that velocity field is not uniform in the turbulent flow. Therefore, the so-called RANS Equations (Reynolds-Averaged Navier-Stokes Equations) has been driven from the unsteady form of NS equations, by considering a time-average on the latter. The x-direction term of momentum eq. is described in equation (2-2):

$$\rho \left(\frac{\partial}{\partial x} (\bar{u}^2) + \frac{\partial}{\partial y} (\bar{u}\bar{v}) \frac{\partial}{\partial z} (\bar{u}\bar{w}) \right) = -\frac{\partial \bar{p}}{\partial x} + \left[\frac{\partial}{\partial x} \left(\mu \frac{\partial \bar{u}}{\partial x} - \rho \overline{u'^2} \right) + \frac{\partial}{\partial y} \left(\mu \frac{\partial \bar{u}}{\partial y} - \rho \overline{u'v'} \right) + \frac{\partial}{\partial z} \left(\mu \frac{\partial \bar{u}}{\partial z} - \rho \overline{u'w'} \right) \right] \quad (2-2)$$

Where $u = \bar{u} + u'$ and the time average of u' is zero (the same for v and w). $\mu \frac{\partial \bar{u}}{\partial x}$ is the viscous normal stress in a laminar flow, the quantity $\rho \overline{u'^2}$ may be termed the normal stress due to turbulence.

The Navier-Stokes equations are extremely difficult to solve analytically. During the 20th century, numerical methods has been used to find the viable solutions for the Navier-Stokes

equations and it became possible to solve them by numerical simulations. The key to solve Navier-Stokes equations numerically is to discretize the infinite field to a finite set of points, elements or volumes. The common discretization methods are:

- Finite Difference Method

The infinite set of points is replaced by a finite set of points, called nodes, and the Navier-Stokes equations are applied at these points. The local form of the equations takes the shape of stencils which relate velocity and pressure values at one node to the values at neighboring nodes. Formation of the stencils requires that the nodes be connected in a structured mesh, so that each node can identify its neighbors to the south, north, east, west etc.

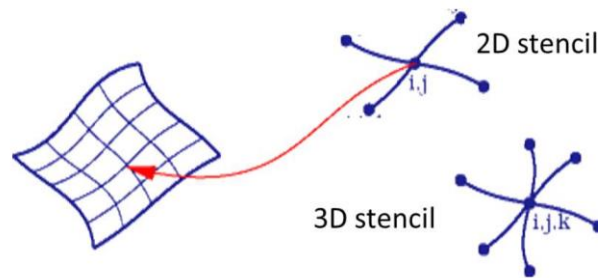


Figure 2-1 A schematic of Finite Difference Method [24]

- Finite Element Method

A large but finite number of known functions are proposed as the representation of the flow field, and Navier-Stokes equations are used to select the one with best approximation properties. The candidate functions are constructed from simple interpolation functions within each element into which the domain is divided. The value of the function everywhere inside the element is determined by values at the nodes of that element. The elements combine to form a mesh, which can be also unstructured.

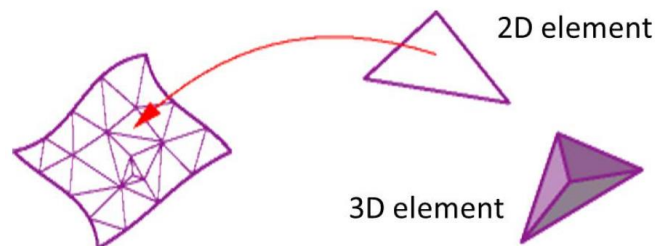


Figure 2-2 A schematic of Finite Element Method [24]

- Finite Volume Method

The volume taken by the fluid is divided into a finite number of volumes or cells, and Navier-Stokes equations are converted into equivalent integral form and are applied to each

cell. The local form of the equations balances mass and momentum fluxes across the faces of each individual cell. The shape of the cells may be irregular, or unstructured.

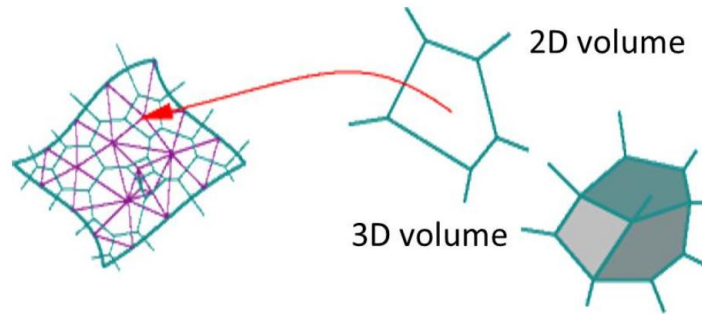


Figure 2-3 A schematic of Finite Volume Method [24]

By applying any of these methods, it is possible to reach better approximation of the actual solution of Navier-Stokes equation which is in another word, convergence of the approximate solution to the real solution. Although, it should be considered, by growing number of nodes, the computing time also increase [24].

The aim in OpenFOAM is to offer an unrestricted choice to the user, starting with the choice of discretization practice which is generally standard Gaussian finite volume integration. Gaussian integration is based on summing values on cell faces, which must be interpolated from cell centers. The *Gauss* entry specifies the standard finite volume discretization of Gaussian integration which requires the interpolation of values from cell centers to face centers. The interpolation scheme is then given by the *linear* entry, meaning linear interpolation or central differencing [35]. The standard finite volume discretization and linear interpolation (*Gauss linear*) has been used in this study.

2.2 ICEM

ANSYS ICEM CFD provides advanced geometry acquisition, mesh generation, and mesh optimization tools to meet the requirement for integrated mesh generation for today's sophisticated analyses. Maintaining a close relationship with the geometry during mesh generation, ANSYS ICEM CFD is used especially in engineering applications such as computational fluid dynamics and structural analysis.

The generic working process involves the following steps and can be seen in Figure (2-4):

- Open/Create a project.
- Create/Manipulate the geometry.
- Create the mesh.
- Check/Edit the mesh.
- Generate the input for the solver.

As the meshing tool of OpenFOAM is not very capable in the meshing of complex geometries, ANSYS ICEM CFD 16.2 has been used for meshing and the output has been translated into OpenFOAM format for the simulations.

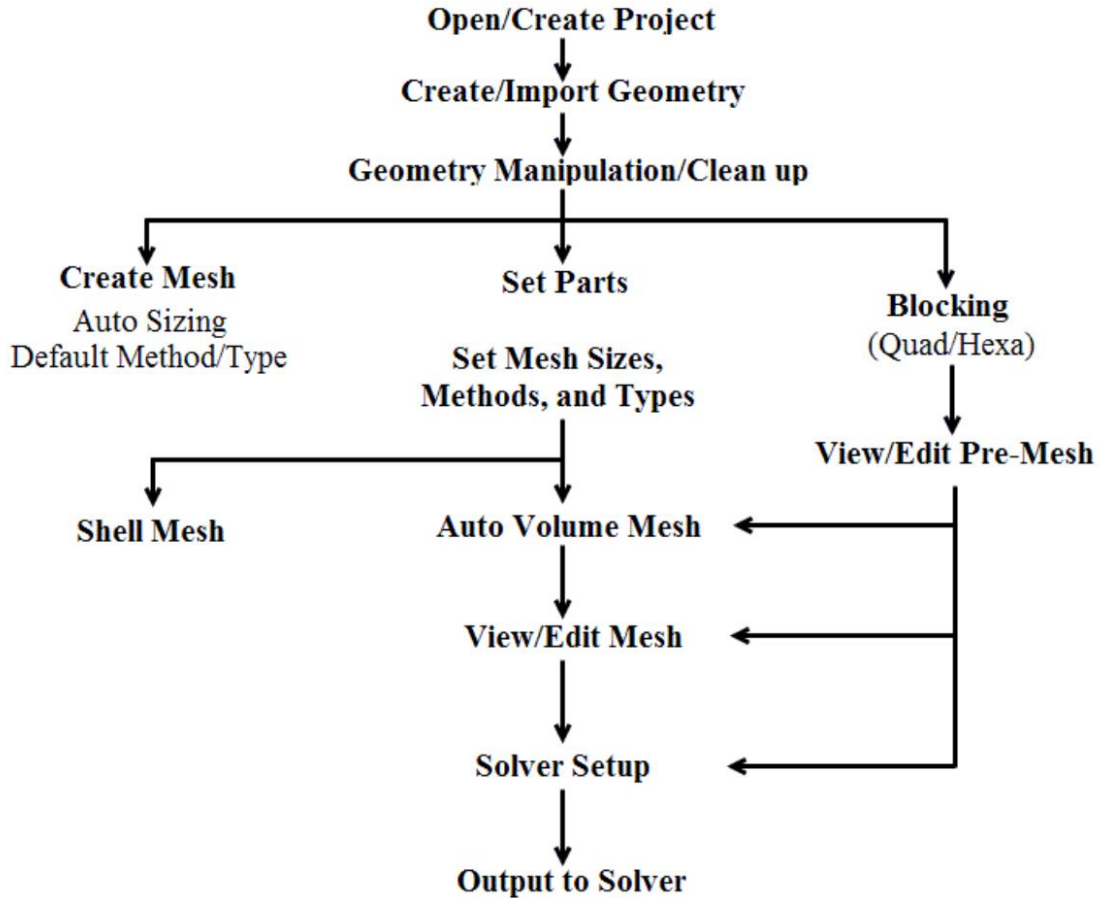


Figure 2-4 The overall process in ICEM

2.3 OpenFOAM

OpenFOAM is an acronym which stands for "Open source Field Operation and Manipulation" and is an open source numerical simulation software with extensive capabilities in solving fluid flows and other multi-physics problems. From the beginning (circa 1993) the software was called simply FOAM and was first developed as part of a PhD project at Imperial College London. In 2004 it became open source under the GNU GPL license and changed name to OpenFOAM. Today it is developed by SGI and widely used by both academic institutions and corporations worldwide.

In this study the full set of equations, that is the continuity equation, Navier–Stokes equation and energy equation were solved using the CFD code in OpenFOAM 2.3.0 (OpenFOAM Foundation, 2014).

2.4 Turbulence modelling

A turbulence model is a computational procedure to close the system of flow equations derived above so that a wide variety of flow problems can be calculated adopting the numerical methods [26]. There are various kinds of turbulence models existing. Each one of them has specific features that makes it appropriate for a special type of problems. In order to choose the turbulence model matching the best with our project, we take a look at the similar works that have already been done.

Shih in [27] has modeled $k - \varepsilon$ realizable turbulence model as a new eddy viscosity model for high Reynolds number turbulent flows and has compared its results with standard $k - \varepsilon$ and experimental data for different flows including the flat plate boundary layer flow and has concluded realizable $k - \varepsilon$ can perform well for this variety of flows.

In [28] Rahman et al. have numerically investigated the unsteady flow past a cylinder by applying Finite Volume Method using different turbulence models and as a result they have supported realizable $k - \varepsilon$ turbulence model as an effective model for visualization of vortex shedding and recommended $k - \omega$ SST model for high Reynolds number flows.

An et al. have investigated the sensitivity of inflow boundary conditions and turbulent profiles through building obstacles in [29] and as a result, they have supported realizable $k - \varepsilon$ model in predicting wind velocities in the high wind regions and stated that the model generally is capable of generating a robust wind field simulation.

Therefore, supported by Shih, An, Fung and Yim, realizable $k - \varepsilon$ is chosen as the main turbulence model and suggested by Rahman, the results are compared for one case with $k - \omega$ SST. These two models are both in the group of two-equation turbulence models.

Two-equation turbulence models are one of the most common type of turbulence models. Models like the $k - \varepsilon$ model and the $k - \omega$ model have become industry standard models and are commonly used for most types of engineering problems. Two equation turbulence models are also very much still an active area of research and new refined two-equation models are still being developed.

By definition, two equation models include two transport equations to represent the turbulent properties of the flow. This allows a two-equation model to account for e. g. convection and diffusion of turbulent energy.

Most often one of the transported variables is the turbulence kinetic energy. The second transported variable varies depending on what type of two-equation model it is. Common choices are the turbulent dissipation, or the specific dissipation. The second variable can be thought of as the variable that determines the scale of the turbulence (length-scale or time-scale), whereas the first variable, determines the energy in the turbulence.

In the two equations category there are two most important and predominant models known as $k - \varepsilon$ and $k - \omega$ models. In the $k - \varepsilon$ model again there are three kinds of standard, realizable and *RNG* $k - \varepsilon$ models. However, the basic equation is only the $k - \varepsilon$, the other two are the later corrections or improvements in the basic model. As it was already

considered that the realizable $k - \varepsilon$ is used as the base turbulence model in this study, the standard and realizable $k - \varepsilon$ models will be introduced. In the $k - \omega$ models, again there are three kinds of Standard, Wilcox's modified and $k - \omega$ SST model. For this group also, introduction will be on Standard and SST models.

2.4.1 Standard $k - \varepsilon$

The turbulence kinetic energy, k is obtained from the following equation:

$$\frac{\partial}{\partial t}(\rho k) + \frac{\partial}{\partial x_i}(\rho k u_i) = \frac{\partial}{\partial x_j} \left[\left(\mu + \frac{\mu_t}{\sigma_k} \right) \frac{\partial k}{\partial x_j} \right] + P_k + P_b - \rho \varepsilon - Y_M \quad (2-3)$$

while the dissipation rate, ε can be obtained from the equation below:

$$\frac{\partial}{\partial t}(\rho \varepsilon) + \frac{\partial}{\partial x_i}(\rho \varepsilon u_i) = \frac{\partial}{\partial x_j} \left[\left(\mu + \frac{\mu_t}{\sigma_\varepsilon} \right) \frac{\partial \varepsilon}{\partial x_j} \right] + C_{1\varepsilon} \frac{\varepsilon}{k} (P_k + C_{3\varepsilon} P_b) - C_{2\varepsilon} \rho \frac{\varepsilon^2}{k} \quad (2-4)$$

In the above equation, the term

$$P_k = -\rho u'_i u'_j \frac{\partial u_j}{\partial x_i} \quad (2-5)$$

represents the generation of turbulence kinetic energy due to the mean velocity gradients and is common in many of the turbulence models. This equation, considering Boussinesq hypothesis can be also redefined as:

$$P_k = \mu_t S^2 \quad (2-6)$$

where S is the modulus of mean rate-of-strain tensor and is defined as,

$$S = \sqrt{2S_{ij}S_{ij}} \quad (2-7)$$

and

$$S_{ij} = \frac{1}{2} \left(\frac{\partial u_i}{\partial x_j} + \frac{\partial u_j}{\partial x_i} \right) \quad (2-8)$$

P_b is the generation of turbulence kinetic energy due to buoyancy and Y_m represents the contribution of compressibility which as we are not considering the buoyancy or compressibility, it is possible to neglect both of these variables. The turbulent viscosity at each point is related to the local values of turbulence kinetic energy and its dissipation rate by:

$$\mu_t = \rho C_\mu \frac{k^2}{\varepsilon} \quad (2-9)$$

$C_{1\varepsilon}$, $C_{2\varepsilon}$, $C_{3\varepsilon}$ and C_μ are constants that have been determined experimentally and are taken to have the following values:

$$C_{1\varepsilon} = 1.44, C_{2\varepsilon} = 1.92, C_{3\varepsilon} = -0.33, C_\mu = 0.09 \quad (2-10)$$

σ_k and σ_ε are turbulent Prandtl numbers for the turbulence kinetic energy and its dissipation rate. These have also been derived experimentally and are defined as follows:

$$\sigma_k = 1.0, \sigma_\varepsilon = 1.3 \quad (2-11)$$

2.4.2 Realizable $k - \varepsilon$

The Realizable model by Shih et al. [27], is the most recently developed of $k - \varepsilon$ variations and has two main differences with standard $k - \varepsilon$ model. It uses a new equation for the turbulent viscosity. The dissipation rate transport equation has been derived from the equation for the transport of the mean-square vorticity fluctuation. This makes the realizable model more precise than other $k - \varepsilon$ models at predicting flows such as separated flows and flows with complex secondary flow features [27].

The transport equations in this model are as followed:

$$\frac{\partial}{\partial t}(\rho k) + \frac{\partial}{\partial x_i}(\rho k u_i) = \frac{\partial}{\partial x_j} \left[\left(\mu + \frac{\mu_t}{\sigma_k} \right) \frac{\partial k}{\partial x_j} \right] + P_k + P_b - \rho \varepsilon - Y_M \quad (2-12)$$

$$\frac{\partial}{\partial t}(\rho \varepsilon) + \frac{\partial}{\partial x_i}(\rho \varepsilon u_i) = \frac{\partial}{\partial x_j} \left[\left(\mu + \frac{\mu_t}{\sigma_\varepsilon} \right) \frac{\partial \varepsilon}{\partial x_j} \right] + \rho C_1 S_\varepsilon - \rho C_2 \frac{\varepsilon^2}{k + \sqrt{\nu \varepsilon}} + C_{1\varepsilon} \rho \frac{\varepsilon}{k} C_{3\varepsilon} P_b \quad (2-13)$$

where $C_1 = \max[0.43, \frac{\eta}{\eta+5}]$, $\eta = S \frac{k}{\varepsilon}$ and S was defined in equation (2-7).

In transport equations, again P_k represents the generation of turbulence kinetic energy due to mean velocity gradients and is calculated via equation 3.8. P_b is generation of turbulence kinetic energy due to buoyancy, and Y_M represents the fluctuating dilation in compressible turbulence that contributes to the overall dissipation rate. P_b and Y_M are neglected.

The turbulent viscosity is determined by the formula given below in which C_μ is not constant any more.

C_μ is calculated by:

$$C_\mu = \frac{1}{A_0 + A_s \frac{k U^*}{\varepsilon}} \quad (2-14)$$

Where

$$U^* = \sqrt{S_{ij} S_{ij} + \Omega_{ij} \tilde{\Omega}_{ij}} \quad (2-15)$$

And

$$\Omega_{ij} \tilde{\Omega}_{ij} = \Omega_{ij} - 2\varepsilon_{ijk} \omega_k \quad (2-16)$$

And

$$\Omega_{ij} = \overline{\Omega_{ij}} - \varepsilon_{ijk} \omega_k \quad (2-17)$$

In the above equation, Ω_{ij} is the mean rate of rotation tensor viewed in a rotating reference frame with angular velocity ω_k . The constants A_0 and A_s are defined as;

$$A_0 = 4.04, A_s = \sqrt{6} \cos \varphi \quad (2-18)$$

where

$$\varphi = \frac{1}{3} \cos^{-1}(\sqrt{6}W), W = \frac{S_{ij}S_{jk}S_{ki}}{S^3}, S = \sqrt{2S_{ij}S_{ij}} \quad (2-19)$$

And

$$S_{ij} = \frac{1}{2} \left(\frac{\partial u_i}{\partial x_j} + \frac{\partial u_j}{\partial x_i} \right) \quad (2-8)$$

It has been shown that C_μ is a function of the mean strain and rotational rates, the angular velocity of the rotating system, and the turbulence kinetic energy and its dissipation rate.

$C_{1\varepsilon}$ and $C_{3\varepsilon}$ have been defined in equation (2-10). The other constants in this model are defined as below:

$$C_2 = 1.9, \sigma_k = 1.0, \sigma_\varepsilon = 1.2 \quad (2-20)$$

2.4.3 Standard $k - \omega$

The standard $k - \omega$ model is the basic one of the $k - \omega$ turbulence models which was developed by Wilcox [32]. This model is an empirical based model with transport equations for k and ω and has been modified several times to improve accuracy.

The transport equations for this model are as followed:

$$\frac{\partial}{\partial t}(\rho k) + \frac{\partial}{\partial x_i}(\rho k u_i) = \frac{\partial}{\partial x_i} \left[\left(\mu + \frac{\mu_t}{\sigma_k} \right) \frac{\partial k}{\partial x_j} \right] + P_k + Y_k \quad (2-21)$$

$$\frac{\partial}{\partial t}(\rho \omega) + \frac{\partial}{\partial x_i}(\rho \omega u_i) = \frac{\partial}{\partial x_j} \left[\left(\mu + \frac{\mu_t}{\sigma_\omega} \right) \frac{\partial \omega}{\partial x_j} \right] + P_\omega - Y_\omega \quad (2-22)$$

where P_k is the generation of turbulence kinetic energy due to mean velocity gradients which is found with equation (2-5) and P_ω is generation of ω . Y_k and Y_ω represent the dissipation of k and ω due to turbulence. σ_k and σ_ω are the turbulent Prandtl numbers (constants in this case; equal to 2) for k and ω respectively.

The turbulent viscosity is defined using a damping coefficient (α^*);

$$\mu_t = \alpha^* \frac{\rho k}{\omega} \quad (2-23)$$

The low-Reynolds number correlation is obtained from this coefficient which is given by,

$$\alpha^* = \alpha_\infty^* \left(\frac{\alpha_0^* + \frac{Re_t}{R_k}}{1 + \frac{Re_t}{R_k}} \right) \quad (2-24)$$

where $Re_t = \frac{\rho k}{\mu \omega}$, $R_k = 6$, $\alpha_0^* = \frac{\beta_i}{3}$, $\beta_i = 0.072$ and $\alpha_\infty^* = 1$. For the high Reynolds form of the standard $k - \omega$ model, $\alpha^* = \alpha_\infty^* = 1$.

P_ω is defined as:

$$P_\omega = \frac{\alpha}{\nu_t} P_k \quad (2-25)$$

The coefficient α is given by:

$$\alpha = \frac{\alpha_\infty}{\alpha^*} \left(\frac{\alpha_0^* + \frac{Re_t}{R_k}}{1 + \frac{Re_t}{R_k}} \right) \quad (2-26)$$

in which $R_\omega = 2.95$. The equation for α_∞ in this model is:

$$\alpha_\infty = F_1 \alpha_{\infty,1} + (1 - F_1) \alpha_{\infty,2} \quad (2-27)$$

where

$$\alpha_{\infty,1} = \frac{\beta_{i,1}}{\beta_\infty^*} - \frac{\kappa^2}{\sigma_{\omega,1} \sqrt{\beta_\infty^*}} \quad (2-28)$$

$$\alpha_{\infty,2} = \frac{\beta_{i,2}}{\beta_\infty^*} - \frac{\kappa^2}{\sigma_{\omega,2} \sqrt{\beta_\infty^*}} \quad (2-29)$$

The term Y_k is defined as

$$Y_k = \rho \beta^* f_{\beta^*} k \omega \quad (2-30)$$

and the term for the dissipation of ω due to turbulence, Y_ω is defined as

$$Y_\omega = \rho \beta^* f_\beta k \omega \quad (2-31)$$

The terms f_β and f_{β^*} are hard to be defined for standard model, but they have constant values for the next model.

2.4.4 $k - \omega$ SST

The second one of $k - \omega$ models which is introduced in this study is the shear stress transport (SST) model which was developed by Menter [30] using the standard model and a transformed $k - \varepsilon$ model and differs from the standard model specially in the way which the model calculates the turbulent viscosity. This model also incorporates a blending function to allow proper calculation of the near wall and far field areas by triggering the standard $k - \omega$ model in near wall regions and the $k - \varepsilon$ model away from walls. These differences make the SST model more precise for a larger variety of flows than the standard model [30], [31].

The transport equations for k and ω are slightly modified and are given by,

$$\frac{\partial}{\partial t} (\rho k) + \frac{\partial}{\partial x_i} (\rho k u_i) = \frac{\partial}{\partial x_i} \left[\left(\mu + \frac{\mu_t}{\sigma_k} \right) \frac{\partial k}{\partial x_j} \right] + P_k + Y_k \quad (2-32)$$

$$\frac{\partial}{\partial t} (\rho \omega) + \frac{\partial}{\partial x_i} (\rho \omega u_i) = \frac{\partial}{\partial x_j} \left[\left(\mu + \frac{\mu_t}{\sigma_\omega} \right) \frac{\partial \omega}{\partial x_j} \right] + P_\omega - Y_\omega + D_\omega \quad (2-33)$$

where P_k represents the generation of turbulence kinetic energy due to mean velocity gradients, P_ω is generation of ω defined by equation (2-25), and Y_k and Y_ω represent the dissipation of k and ω due to turbulence. σ_k and σ_ω are the turbulent Prandtl numbers for k and ω respectively. The term for production of turbulence kinetic energy, P_k^\sim is determined slightly differently from the other models and is defined as,

$$P_k^\sim = \min(P_k, 10\rho\beta^*k\omega) \quad (2-34)$$

Where P_k is defined in equation (2-6).

The terms for the dissipation of k and ω due to turbulence, Y_k and Y_ω , are defined according to equations (2-30) and (2-31) and in this model f_{β^*} and f_β are both constants with a value of 1. β for high Reynolds incompressible flow of our case is equal to β_i which for *SST* model is defined as:

$$\beta_i = F_1\beta_{i,1} + (1 - F_1)\beta_{i,2} \quad (2-35)$$

The turbulent viscosity in this model is calculated by;

$$\mu_t = \frac{a_1\rho k}{\max(a_1\omega, W^\sim F_2)} \quad (2-36)$$

in which W^\sim is the vorticity magnitude $W^\sim = \sqrt{2W_{ij}W_{ij}}$ with:

$$W_{ij} = \frac{1}{2} \left(\frac{\partial u_i}{\partial x_j} - \frac{\partial u_j}{\partial x_i} \right) \quad (2-37)$$

The turbulent Prandtl numbers which were constant in the standard model are equated below and incorporate the blending function F_1 which was also used in equation (2-35). The other blending function F_2 was used above in the equation (2-36). Blending functions have been added to the *SST* model to ensure that the model equations behave appropriately in both near wall and far field zones.

$$\sigma_k = \frac{1}{F_1/\sigma_{k,1} + (1-F_1)/\sigma_{k,2}} \quad (2-38)$$

$$\sigma_\omega = \frac{1}{F_1/\sigma_{\omega,1} + (1-F_1)/\sigma_{\omega,2}} \quad (2-39)$$

where:

$$F_1 = \tanh(\Phi_1^4), \quad F_2 = \tanh(\Phi_2^2) \quad (2-40)$$

in which,

$$\Phi_1 = \min \left[\max \left(\frac{\sqrt{k}}{\beta^*\omega y}, \frac{500\nu}{y^2\omega} \right), \frac{4\rho k}{\sigma_{\omega,2}D_\omega^+ y^2} \right] \quad (2-41)$$

$$D_\omega^+ = \max \left(2\rho \frac{1}{\sigma_{\omega,2}\omega} \frac{\partial k}{\partial x_j} \frac{\partial \omega}{\partial x_j}, 10^{-10} \right) \quad (2-42)$$

and

$$\Phi_2 = \max\left(2 \frac{\sqrt{k}}{\beta^* \omega d}, \frac{500\nu}{y^2 \omega}\right) \quad (2-43)$$

in this equation y is the distance from the field point to the nearest wall.

The cross-diffusion term, D_ω blends the standard $k - \varepsilon$ model and the standard $k - \omega$ model and is defined as

$$D_\omega = 2(1 - F_1)\rho \frac{1}{\sigma_{\omega,2}\omega} \frac{\partial k}{\partial x_j} \frac{\partial \omega}{\partial x_j} \quad (2-44)$$

The constants specific to the *SST* $k - \omega$ model are defined as,

$$\begin{aligned} \sigma_{\omega,1} = 2.0, \quad \sigma_{\omega,2} = 1.168, \quad \sigma_{k,1} = 1.176, \quad \sigma_{k,2} = 1.0, \quad a_1 = 0.31 \\ \beta^* = 0.09, \quad k = 0.41, \quad \beta_{i,1} = 0.075, \quad \beta_{i,2} = 0.0828, \quad \beta_\infty^* = 0.075 \end{aligned} \quad (2-45)$$

2.5 Dimensionless wall distance

The y^+ value is a non-dimensional distance from the wall to the first mesh node. To use a wall function approach for a particular turbulence model with confidence, it is needed to ensure that the y^+ values are within a certain range and not so large that the first node falls outside the boundary layer region. If this happens, then the Wall Functions used by the turbulence model may incorrectly calculate the flow properties at this first calculation point which will introduce errors into the pressure drop and velocity results. The upper range of applicability will vary depending on the flow physics and the extent of the boundary layer profile. Equation (2-46) represents the relationship for calculating y^+ value:

$$y^+ = \frac{u_* \times y}{\nu} \quad (2-46)$$

In this equation, u_* is the friction velocity, y is the first node distance to the nearest wall and ν is the kinematic viscosity.

It is important in turbulence modeling to determine the proper size of the cells near domain walls. The turbulence model wall functions have restrictions on the y^+ value at the wall and if these restrictions are not satisfied, wall functions might not be valid any more. For the $k - \omega$ *SST* that has been used in this study, with high Reynolds number (about 10^7), model requires a wall y^+ value between approx. 1 and 100. A faster flow near the wall will produce higher values of y^+ , so the grid size near the wall must be reduced [32].

3 SIMULATION SETUP

3.1 Geometry

As it has been explained briefly in the chapter 1, the general geometry of this study has been adopted from the work by Felsch et al. (2014) [12]. For a 75 MW thermal power tower, the dimensions of the cavity according to Figure 1-5 would be as follow:

$$d = 18.95 \text{ m}, d_{out} = 24.63 \text{ m}, l = 20.46 \text{ m}, l_{out} = 26.53 \text{ m} \quad (3-1)$$

The geometry has been created in ANSYS Workbench for a better compatibility with the ANSYS ICEM that will be used as the meshing tool in the following.

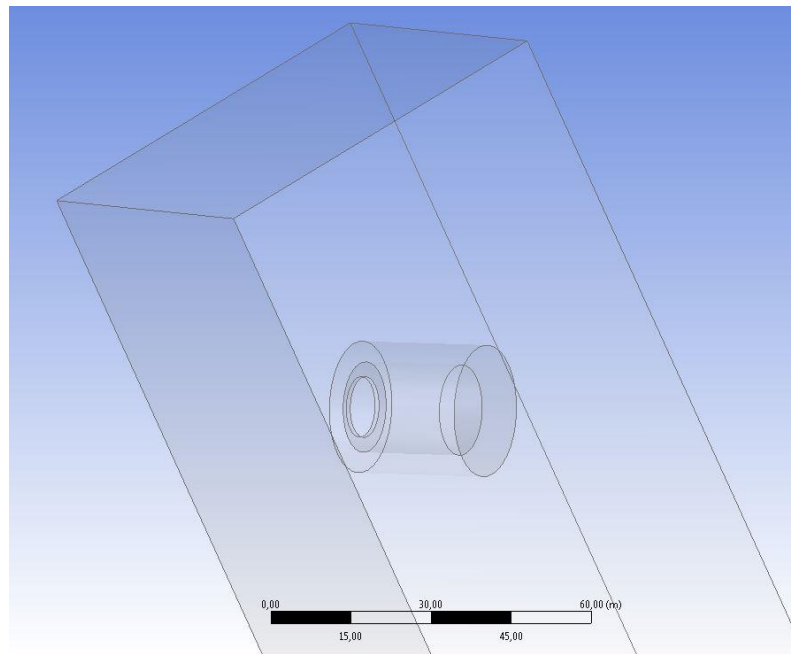


Figure 3-1 Cavity and Wind tunnel geometry, created in ANSYS workbench

To evaluate the effects of wind on the convective heat losses, the cavity has been placed in a wind tunnel with an approximate 10: 1 cross section area ratio (compare to the cavity) to simulate the free flow of an open-air test environment. The dimensions of the wind tunnel for the simulation are as follow according to Figure 3-2:

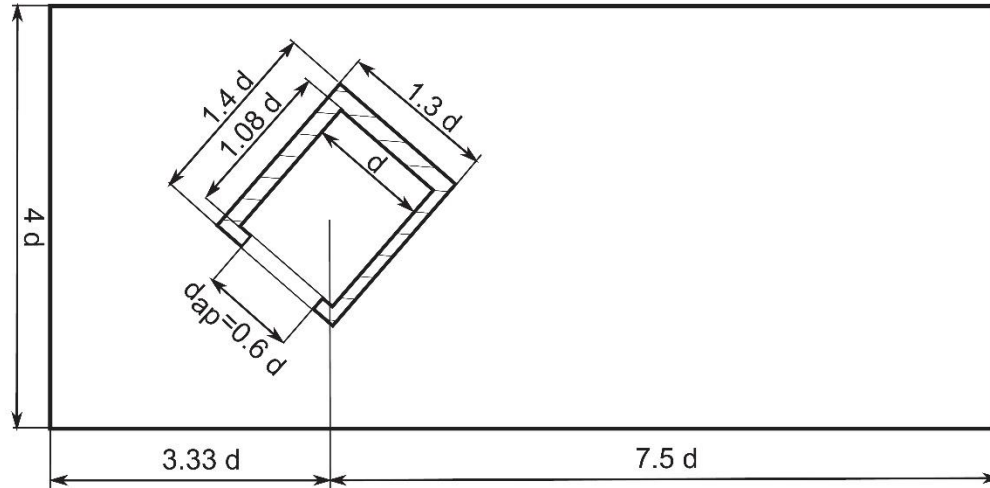


Figure 3-2 Wind tunnel dimensions

Wind tunnel dimensions: 71m × 71m × 185m (3-2)

For the simplicity of the model and as it is shown in Figure 3-1, the cavity has been considered horizontal in this study and instead the wind tunnel and the gravitational forces have been rotated to simulate the real test environment.

3.2 Grid generation

In order to have reliable CFD computations and simulations, generation of a good quality mesh is the key factor. In this study, the focus is on the convicting heat losses from inside the cavity and this will require more focus and elaborations on the meshing inside of the cavity. As we are dealing with dimensions in the order of tens of meters, a good strategy must be defined to ensure that the computational time required for the simulation is in an acceptable order. The mesh generation in study has been done in ANSYS ICEM 16.2 and the simulations has been done on 3 different mesh qualities to ensure that the results are coherent and independent of the meshing.

3.2.1 Topology

As mentioned before, the cavity has been placed in a wind tunnel as shown in Figure 3-2. On the left side is the inlet of the wind tunnel and on the right side is the outlet and the four long sides are the walls of the wind tunnel. Since there is a pressure drop in the wind behind the receiver, we have considered a greater distance from the receiver to the outlet comparing to the inlet, to ensure that the flow can homogenize again in the outlet.

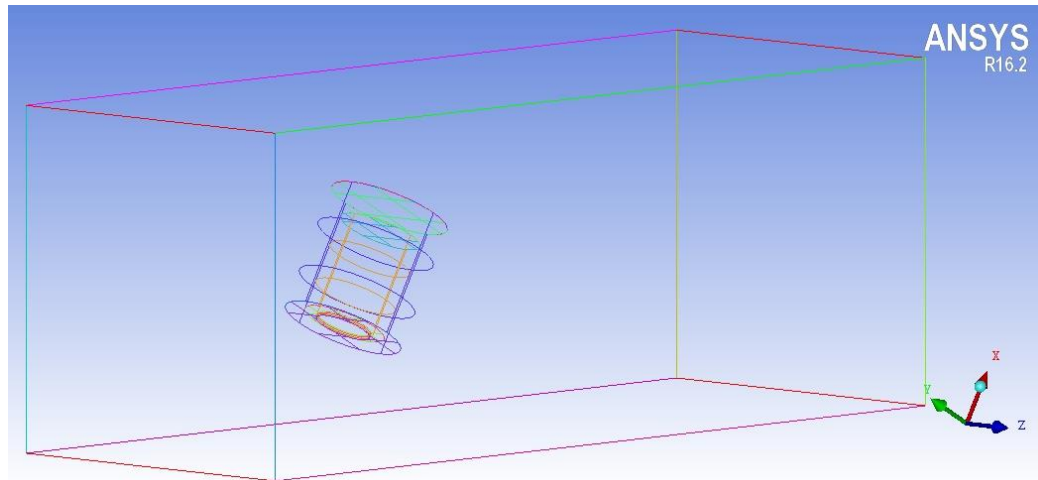


Figure 3-3 Wind tunnel and cavity model in ANSYS ICEM

The blocking feature in ANSYS ICEM CFD provides a projection-based mesh-generation environment. The blocking step is used when a structured, hexa-mesh is desired in one or more parts. A pre-mesh is generated in the blocked regions which can be refined and improved on a block-by-block basis. Using this feature, we could refine our mesh inside the cavity and in the sections that we needed a detail information to study the flow and heat transfer. The pre-mesh data is converted to structured or unstructured mesh data before it is merged with mesh data from other parts or passed to a solver.

There can be multiple Blocking strategies, depending on the topology that is used, and in this study, we used a top-down approach, in which you first capture the outer geometry and then split, delete, and merge blocks to capture the minor geometry. The blocking structure is shown in figure 3-3 and 3-4.

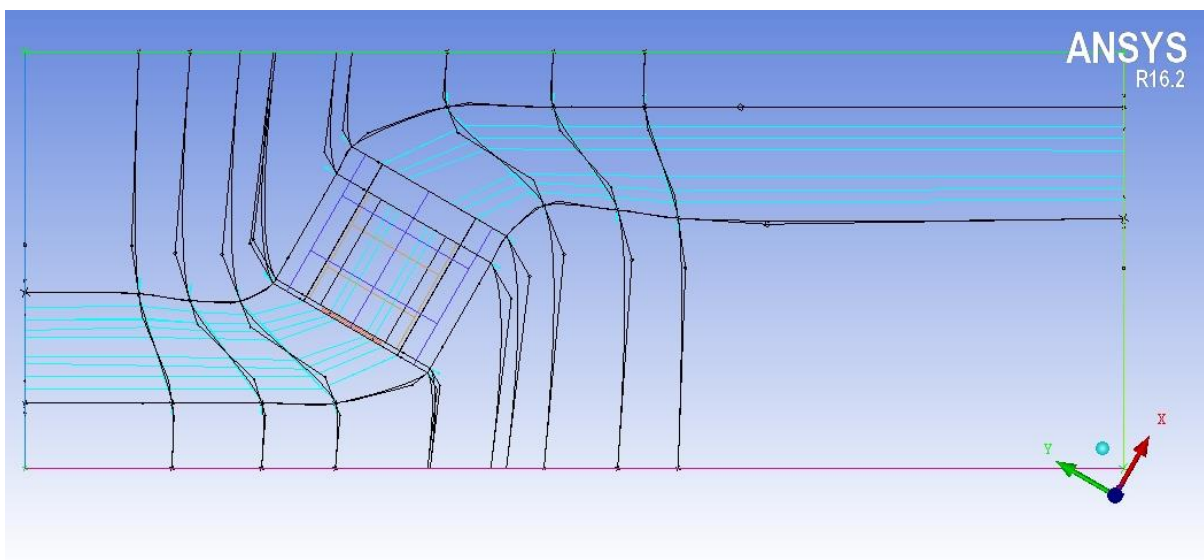


Figure 3-4 Blocking structure - side view

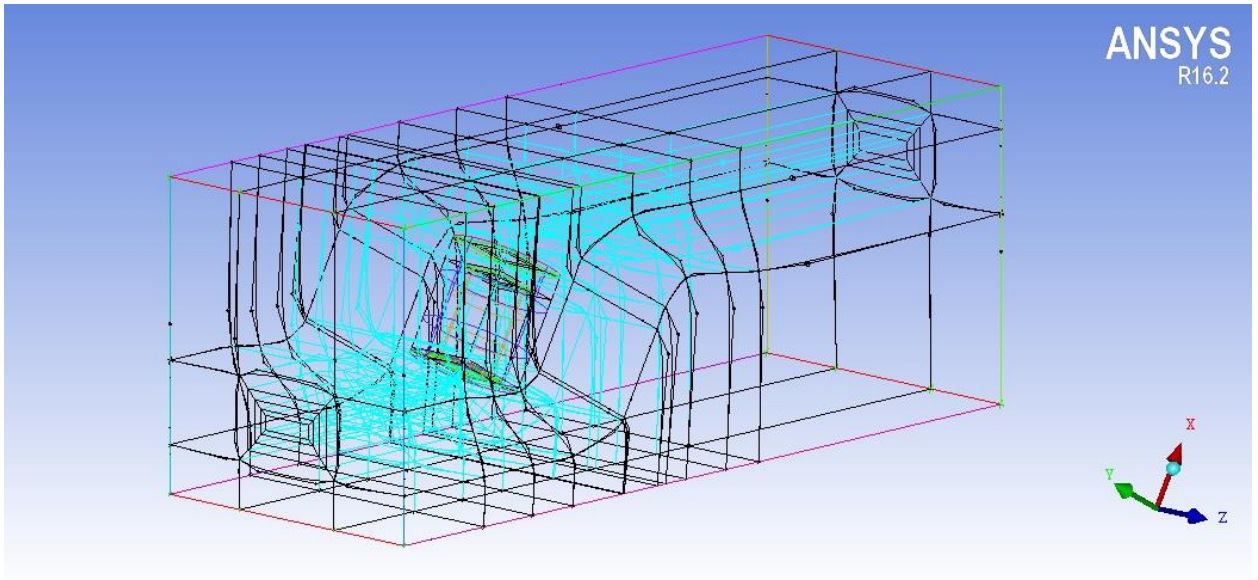


Figure 3-5 Blocking structure - 3D

ANSYS ICEM CFD has a specific O-Grid tool to make it easy to accomplish even for complicated geometries. This is the best method for fixing bad angles in block corners within cylindrical geometry. Required by the cylindrical shape of the receiver in this study, O-Grids has been created for the cavity and on each of the inlet and outlet. The O-grid inside the receiver is shown in Figure 3-3.

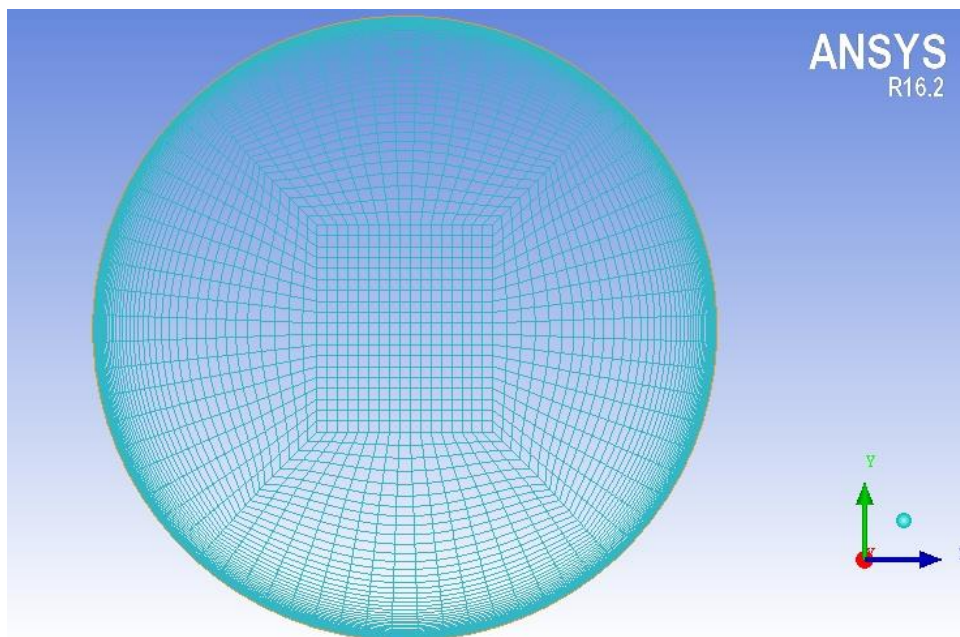


Figure 3-6 O-Grid inside the cavity

3.2.2 Grid Quality

To evaluate the accuracy of the simulations carried out on this study and the independency of the results from the mesh, three different meshes (coarse, medium and fine) has been created and simulated.

Inflated boundary layers are another key point that has been considered in the meshing of this study. As the heat transfer between the internal walls of cavity and air has to be calculated and studied in the thermal boundary layers, we have created an inflated mesh on the boundary layers inside the cavity by specifying the size of the first cell in the boundary layer and specifying the ratio of growth toward the maximum cell size.

As we have used the wall functions for the turbulence modelling in this study, the value of the dimensionless wall distance has been checked for each mesh to have the proper value based on the required range for the wall function.

To check the quality of all meshes generated, they have been checked both in ANSYS ICEM CFD and OpenFOAM using the Check Mesh option available and they are all good. Also, non-orthogonality, as one of the most key factors in the mesh quality has been checked and the results are reported in the following.

The three meshes used in this study has been shown in the following figures:

1. Coarse mesh (M6):
1,075,688 elements with the "Max ortho" diagnostic
 $min = 0^\circ$, $max = 63.3215^\circ$, $mean = 22.6303537829^\circ$

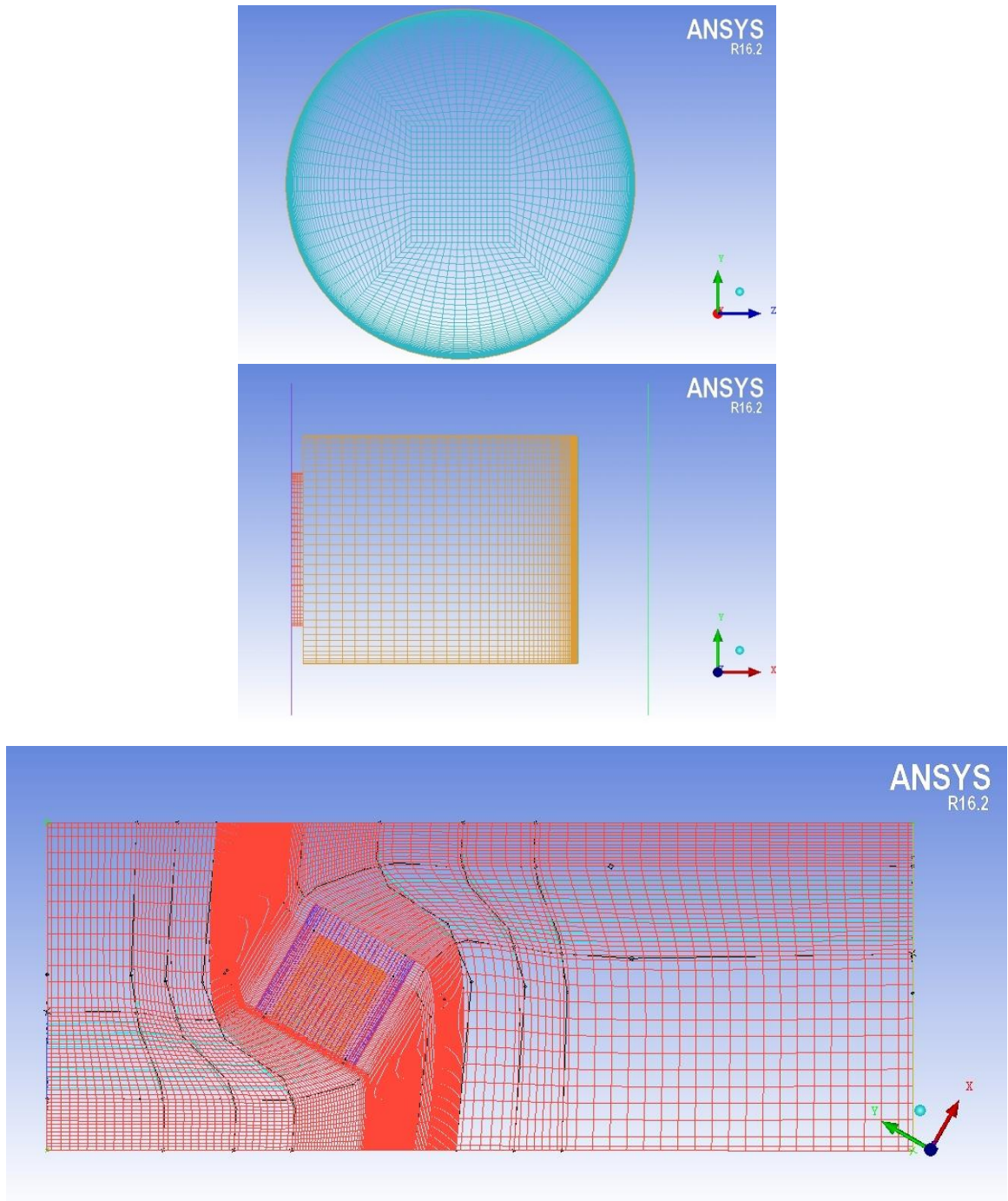


Figure 3-7 Coarse Mesh(M6)

2. Medium mesh (M5):

2,870,954 elements with the "Max ortho" diagnostic

$min = 2.54444e - 014^\circ$, $max = 60.944^\circ$, $mean = 20.6712124263^\circ$

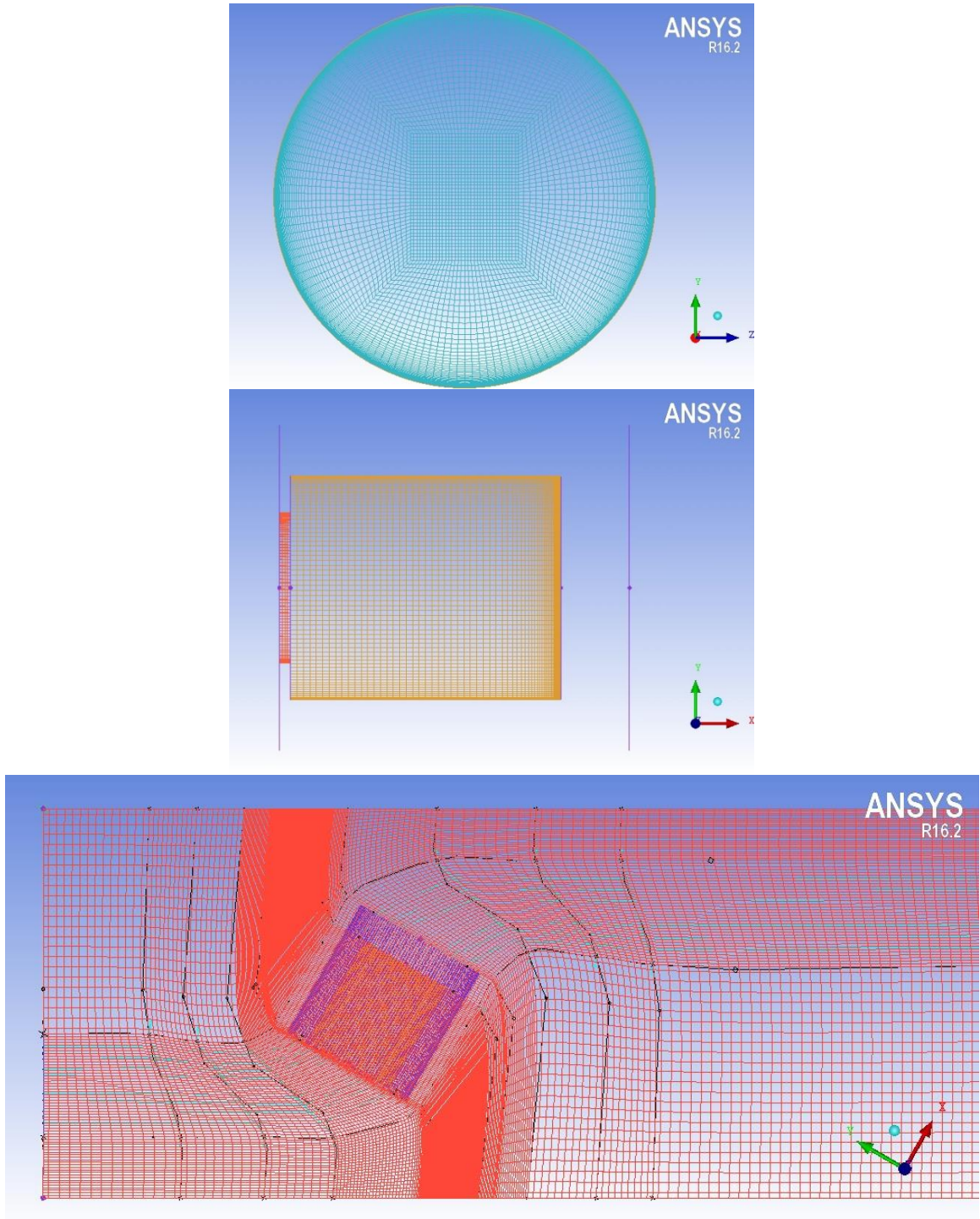


Figure 3-8 Medium mesh (M5)

3. Fine mesh (M4):

10,289,421 elements with the "Max ortho" diagnostic

$min = 0^\circ$, $max = 59.4423^\circ$, $mean = 18.2204615789^\circ$

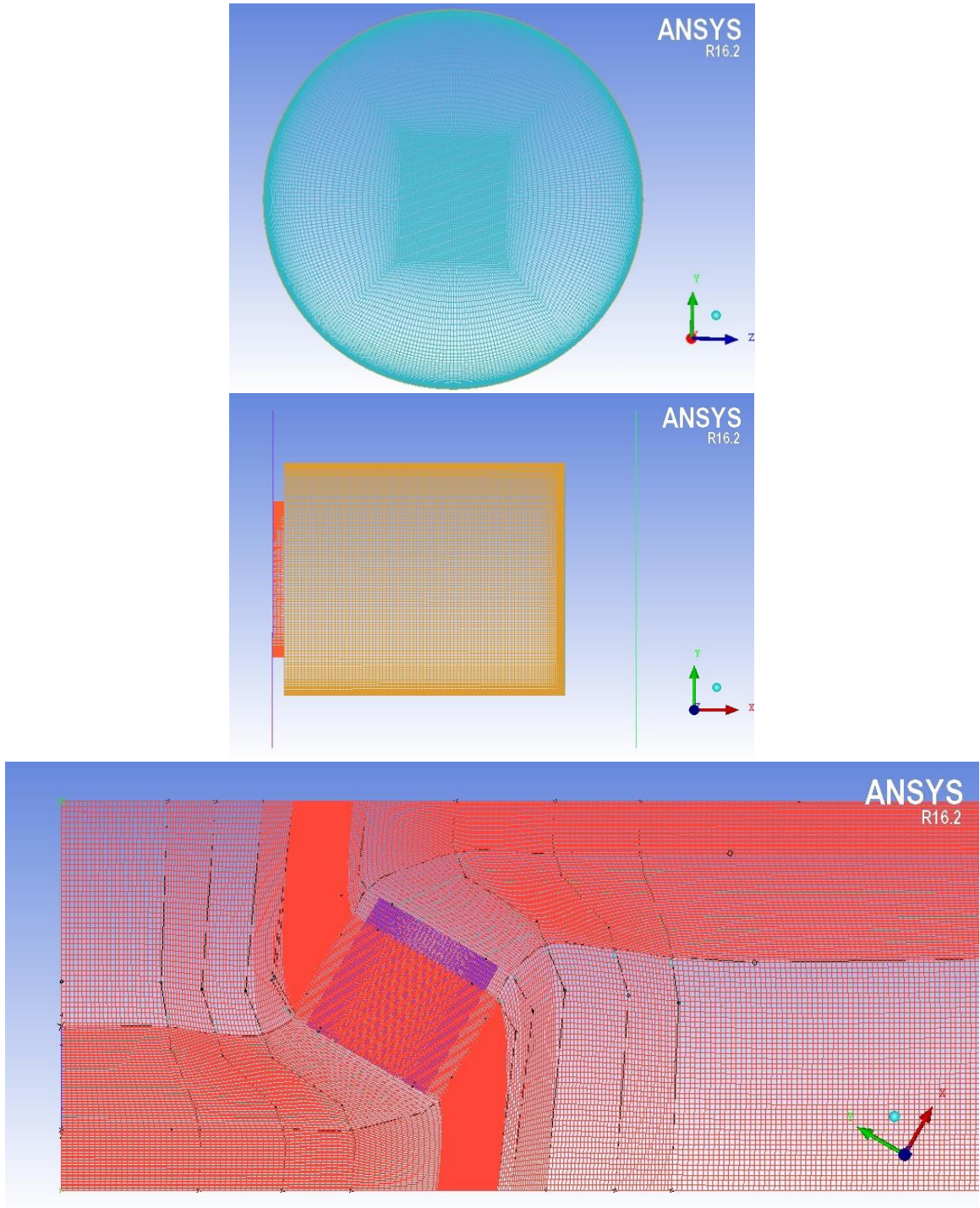


Figure 3-9 Medium mesh (M4)

3.3 Simulation setup

The most important assumptions and configurations used for the numerical simulations in the OpenFOAM will be explained in this section.

3.3.1 Boundary type

Apart from the Inlet and Outlet of the wind tunnel, all the other boundaries have been set as “wall”, as they are solid walls and “wall” boundary type is required for some physical modelling, e.g. wall functions in turbulence modelling.

The Inlet and Outlet of the wind tunnel have been set as “patch” boundaries that is a generic type containing no geometric or topological information about the mesh and usually is used for an inlet or an outlet.

3.3.2 Thermophysical properties

```
thermoType
{
    type                heRhoThermo;
    mixture             pureMixture;
    transport           sutherland;
    thermo              janaf;
    equationOfState     perfectGas;
    specie              specie;
    energy              sensibleEnthalpy;
}
```

Thermophysical models are concerned with energy, heat and physical properties. The “thermophysicalProperties” dictionary is read by any solver that uses the *thermophysical* model library. A thermophysical model is constructed in OpenFOAM as a pressure-temperature $p - T$ system from which other properties are computed.

“type” is chosen as “heRhoThermo” which is for solvers that construct rhoThermo, rhoReactionThermo and multiphaseMixtureThermo.

The “mixture” specifies the mixture composition. The option typically used for thermophysical models without reactions is “pureMixture”, which represents a mixture with fixed composition.

The “transport” modelling concerns evaluating dynamic viscosity μ , thermal conductivity κ and thermal diffusivity α (for internal energy and enthalpy equations). “Sutherland” model calculates μ as a function of temperature T from a Sutherland coefficient A_s and Sutherland temperature T_s , specified by keywords A_s and T_s . μ is calculated according to:

$$\mu = \frac{A_s \sqrt{T}}{1 + T_s/T} \quad (3-3)$$

The thermodynamic models. “thermo”, are concerned with evaluating the specific heat C_p from which other properties are derived. “Janaf” calculates C_p as a function of temperature T from a set of coefficients taken from JANAF tables of thermodynamics. The function is valid between a lower and upper limit in temperature T_l and T_h respectively. Two sets of coefficients are specified, the first set for temperatures above a common temperature T_c (and below T_h), the second for temperatures below T_c (and above T_l). The function relating C_p to temperature is:

$$C_p = R \left(\left(\left((a_4 T + a_3) T + a_2 \right) T + a_1 \right) T + a_0 \right) \quad (3-4)$$

T_l , T_c and T_h in this model were 200K, 1000K and 6000K respectively.

“Perfect gas” has been assumed as the equation of state which means:

$$\rho = \frac{1}{RT} p \quad (3-5)$$

The only option available for the “specie” is “specie” which will indicate the composition of the constituents by their number of moles “nMoles” and molar weight “molWeight”.

And finally, the “energy” variable has been specified as “sensibleEnthalpy”. Usually the sensible form of energy is used for the energy calculations as it is easier to account for possible energy changes due to reactions.

3.3.3 Turbulence Properties

“RASModel” (Reynolds-averaged simulation modeling) has been chosen for the simulation type of the turbulence.

3.3.4 RAS Properties

Among all the possible “RASModel”, “kOmegaSST” has been used in this study for the turbulence modeling.

3.3.5 Initial Values

Below are the initial values for different parameters used in this study:

$$\begin{aligned} \text{mut } (\mu_t) = 0, \quad \text{omega } (\omega) = 0.12, \quad p = 101300 \\ p_{rgh} = 101300, \quad T = 283.15K, \quad \text{alphat } (\alpha_t) = 0, \quad k = 1^{-13} \end{aligned} \quad (3-6)$$

The initial value of U has been obtained by running a *potentialFoam* in the simulation setup and the results has been used as the initial values for U to run the main solver on the original model.

3.3.6 Boundary conditions

μ_t (*mut*): Apart from the CAVITYBACKHOT which is the wall at the end of the cavity, on all the walls the “mutkWallFunction” has been used as the boundary condition.

On the CAVITYBACKHOT as there is very small flow, for a better simulation the “mutLowReWallFunction” has been used.

On the INLET and OUTLET of the wind tunnel the “calculated” is used.

On the walls inside the cavity that there is no inflated mesh generated (front of the cavity and the side walls of aperture) we used “mutUSpaldingWallFunction”. This boundary condition provides a turbulent viscosity condition when using wall functions for rough walls, based on velocity, using Spalding's law to give a continuous μ_t profile to the wall.

ω (*omega*): Apart from the INLET and OUTLET of wind tunnel, “compressible::omegaWallFunction” has been used on all walls.

On the INLET, “compressible::turbulentMixingLengthFrequencyInlet” and on the OUTLET, “zeroGradient” has been used.

p : “calculated” condition is used on all boundaries.

p_{rgh} : Apart from the OUTLET of wind tunnel, “fixedFluxPressure” has been used on all boundaries and on the OUTLET “fixedValue” was used.

T : Apart from the CAVITYBACKHOT, CAVITYINHOT, TUNELWALLS and INLET the rest of boundaries has been set to “zeroGradient”.

TUNELWALLS and INLET have been set as “fixedValue” to a value of 283.15K.

CAVITYBACKHOT and CAVITYINHOT have been set as “uniformFixedValue” to a value that was gradually increasing from 283.15K to 1083.15K in 1600 steps.

U : All the walls have been set as “fixedValue” to a uniform value of (0 0 0). The same used for INLET with uniform value of the wind velocity.

OUTLET has been set to an “inletOutlet” boundary.

α_t (*alphat*): All the boundaries have been set as “calculated”.

κ : All the walls have been set as “compressible::kqRWallFunction”.

INLET has been set as “turbulentIntensityKineticEnergyInlet” and OUTLET has been set as “zeroGradient”.

3.3.7 Solver

potentialFoam: This solver has been used for the initiation of all the simulation in this study to calculate the initial conditions of the domain (U field).

bouyantSimpleFoam: is a steady-state solver for buoyant, turbulent flow of compressible fluids, including radiation (if applicable), and can be used for ventilation and heat-transfer problems. In this study all the simulation with the presence of wind has been solved using this solver.

bouyantPimpleFoam: is a transient solver for buoyant, turbulent flow of compressible fluids and can be used for ventilation and heat-transfer problems. In this study it has been used for some attempts for the simulations without the presence of wind ($U = 0$) and checking some of the converged steady-state simulations.

3.3.8 fvSolution

Relaxation factors: To improve the stability of computation particularly in solving steady-state simulations relaxation factors are applied. These factors are working by limiting the amount which one variable changes from one iteration to the next. The relaxation factor used in these simulations are as follow:

```
relaxationFactors
{
  fields
  {
    rho      1.0;
    p_rgh    0.5;
  }
  equations
  {
    U        0.5;
    h        0.8;
    "(k|epsilon|omega)" 0.5;
  }
}
```

3.4 Determination of convective heat losses

In the simulation the inner cylindrical wall and the end of the cavity are kept at a constant uniform temperature. All other walls are assumed to be adiabatic, because only the convective losses from the inner cavity are in the focus of this study. The convective heat losses of the inner cavity walls are calculated using the surface normal gradient of the Temperature $\frac{dT}{dn}$ and the local conductivity of the fluid λ by the following formula:

$$\dot{Q}_{conv} = \int_{A_{cavity}} \lambda, \left(\frac{dT}{dn} \right), dA \quad (3-7)$$

4 RESULTS AND DISCUSSION

After the physical background has been introduced and the model has been explained in chapter 3, in this chapter the results of simulations will be presented. At the first part, the results of the simulations for different wind velocities and its influence on the cavity are presented. In section 4.2 convective losses from the cavity will be evaluated and an overview on the results will be presented. Then the influence on efficiency will be investigated and finally a mesh sensitivity analyses will be done to see the effects of meshing on the results.

4.1 Wind effects on the cavity

As indicated before, the effects of wind up to a maximum of 19 *m/s* on the cavity has been evaluated in this study and the results for wind velocities of 5 *m/s*, 9 *m/s*, 15 *m/s* and 19 *m/s* are reported in the following. Such wind velocities will lead to below non-dimensional fluid and heat transfer parameters.

$$\bullet \quad Re = \frac{u d}{\nu} = 2.82 \times 10^6 - 1.07 \times 10^7 \quad (4-1)$$

$$\bullet \quad Gr = \frac{\beta (T_w - T_\infty) d^3 g}{\nu^2} = 1.85 \times 10^{13} \quad (4-2)$$

$$\bullet \quad \frac{Re^2}{Gr} = 0.115 - 1.65 \quad (4-3)$$

Some points regarding the following results:

- Results reported in this section are for the Medium Mesh (M5) with almost three million elements.
- The temperature profiles reported are from the lowest part of the cavity to the highest along the temperature report line shown in Figure 4-1.
- Figures has been obtained by ParaFoam command in OpenFOAM and through the open source third party platform Paraview.

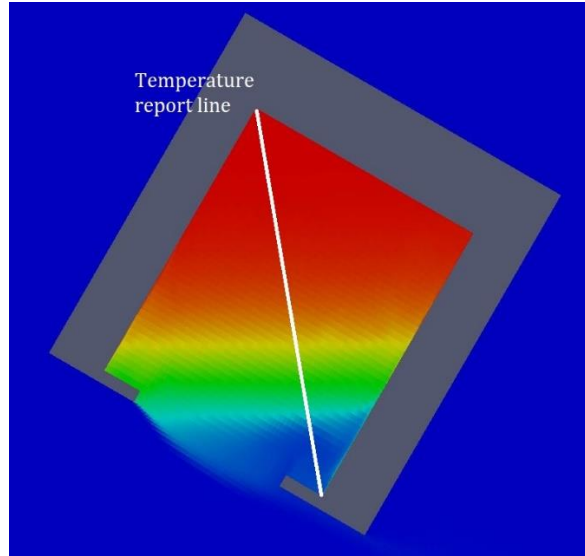


Figure 4-1 Temperature report line

In a zero-velocity test environment, we can expect that the only parameter effecting the convective heat losses is the natural convection happening inside the cavity. As it is also demonstrated in several papers in the literature, a fully developed stagnation zone is expected in the cavity and there would be a natural convection flow from the upper lip of the aperture. Due to the physics of our case in this study, simulating a zero-velocity environment was not fully possible. During several attempts and using a transient solver for zero-velocity simulation, the early stage results were completely in line with expectations and as we can see in Figure 4-2 and 4-3, the stagnation zone has started developing and the natural convection is generating an out flow from the upper lip of the cavity. The following results for zero-velocity has been obtained by simulations conducted on the Mesh number 6 which has the lowest number of elements with a very low temperature difference and in a short period of time (1000 seconds of simulation).

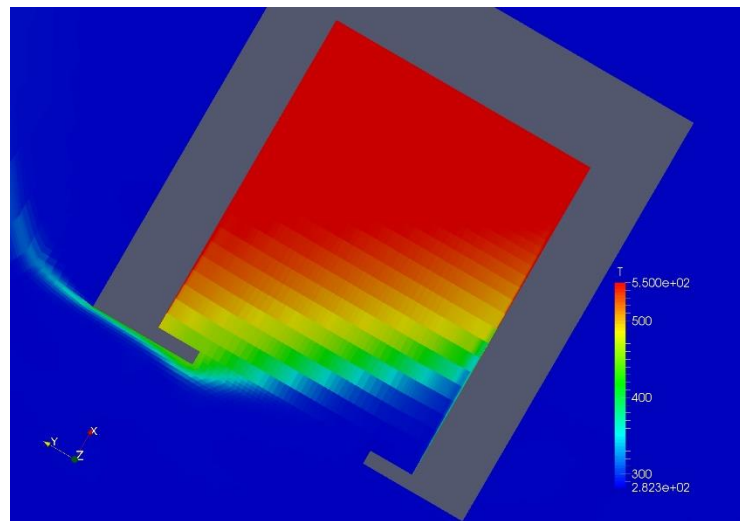


Figure 4-2 Temperature distribution inside cavity ($u = 0$ m/s)

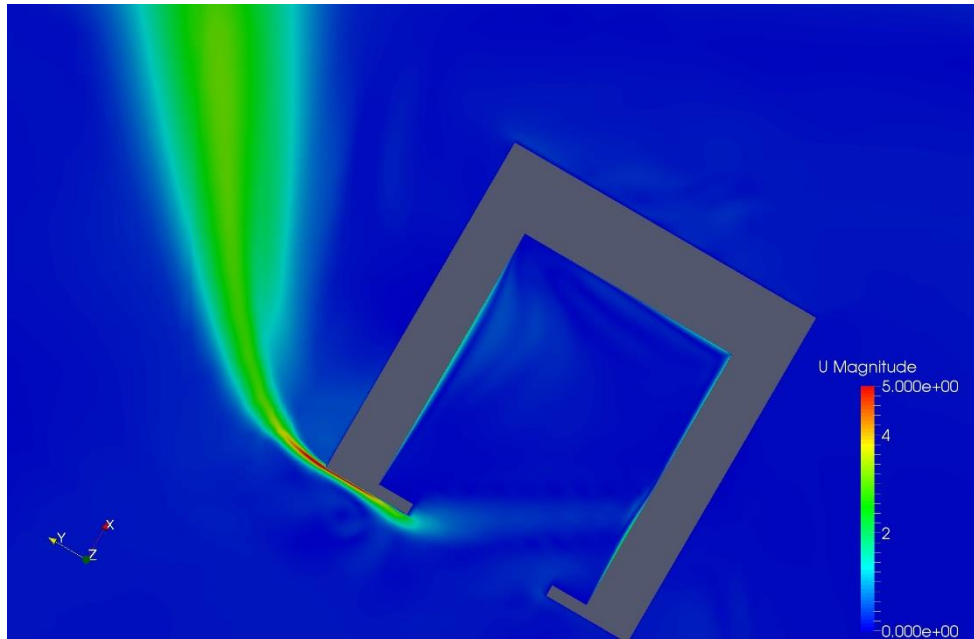


Figure 4-3 Natural convection flow out of Cavity ($u = 0$)

4.1.1 $u = 5 \text{ m/s}$

As it is obvious in the velocity fields (Figure 4-4 and 4-5), there is a small flow almost parallel to the aperture from outside entering the cavity and has produced some small flows inside the cavity. This has affected the stagnation zone and heat transfer inside the cavity. The temperature distribution inside the cavity can be seen in Figure 4-6.

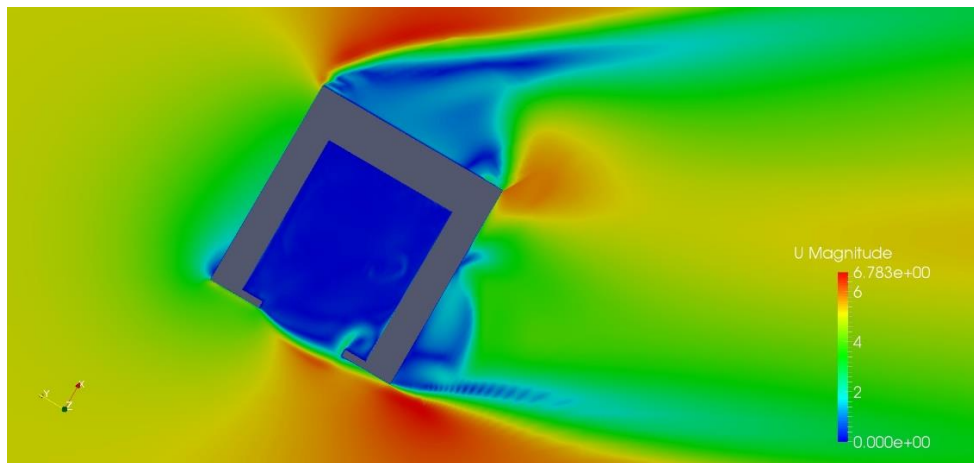


Figure 4-4 Flow field around the cavity ($u = 5 \text{ m/s}$)

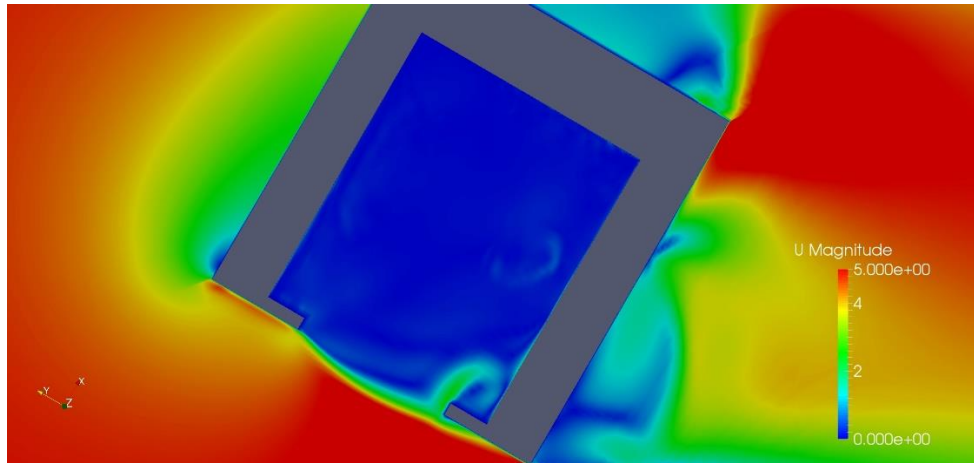


Figure 4-5 Flow field at the aperture ($u = 5 \text{ m/s}$)

As expected the wind is stopping the natural convection flow out of the cavity and there is an interaction between the wind and the natural convection flow in the aperture creating the curve of velocity and temperature in the aperture. Probably a lower wind velocity could have shown the interaction better. In the literature some studies have been reported that a small wind velocity had positive effects on the convective heat losses from the cavity by preventing the heat losses through the natural convection flow out of the cavity.

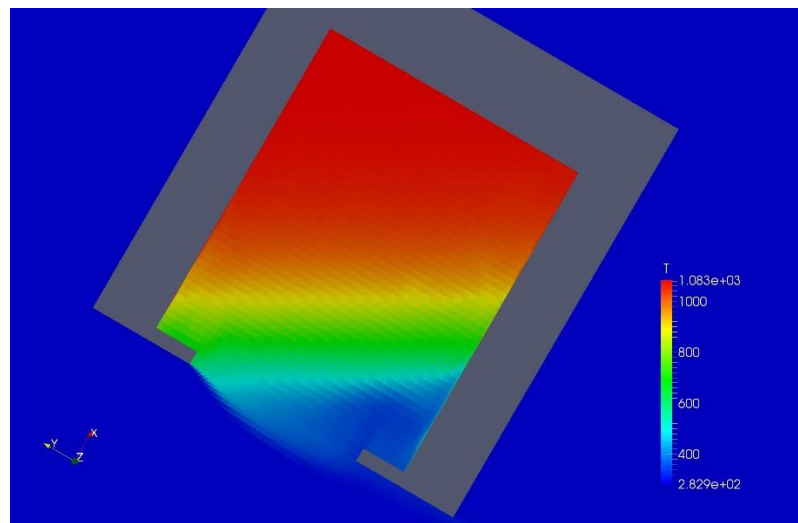


Figure 4-6 Temperature distribution inside cavity ($u = 5 \text{ m/s}$)

The figure below reports the temperature along the cavity. It is obvious that a lower temperature has been obtained in the middle of the cavity and this means that as a boiler, the cavity cannot work efficiently. It is worth to mention that one of the key features of a cavity in this structure could be high uniform temperature in the stagnation zone that can help the efficiency of the cavity as a boiler.

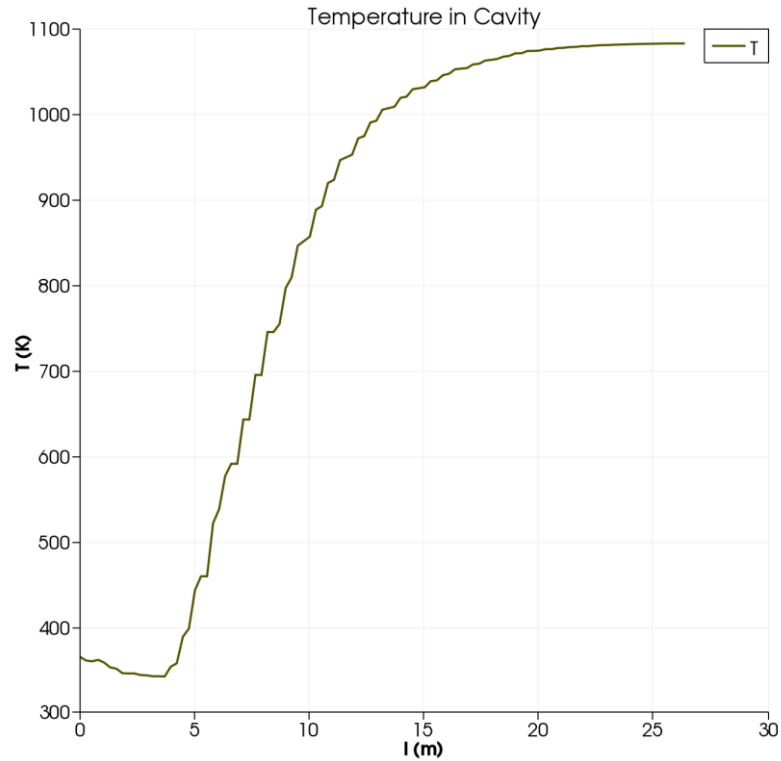


Figure 4-7 Temperature along TRL ($u = 5 \text{ m/s}$)

4.1.2 $u = 9 \text{ m/s}$

Higher velocity of wind in this case has shown a stronger effect of the wind in the interaction of the wind and natural convection flow in the aperture. The interaction curve has been pushed inside the cavity and is almost parallel to the aperture. As shown in Figure 4-9, the wind started flowing inside the cavity from the lower part of it with a higher velocity and inertia. As we also see inside the cavity there are some flows with a low velocity up to the middle of cavity that will defiantly disturb the stagnation zone and increase the heat exchange between the air and the walls.

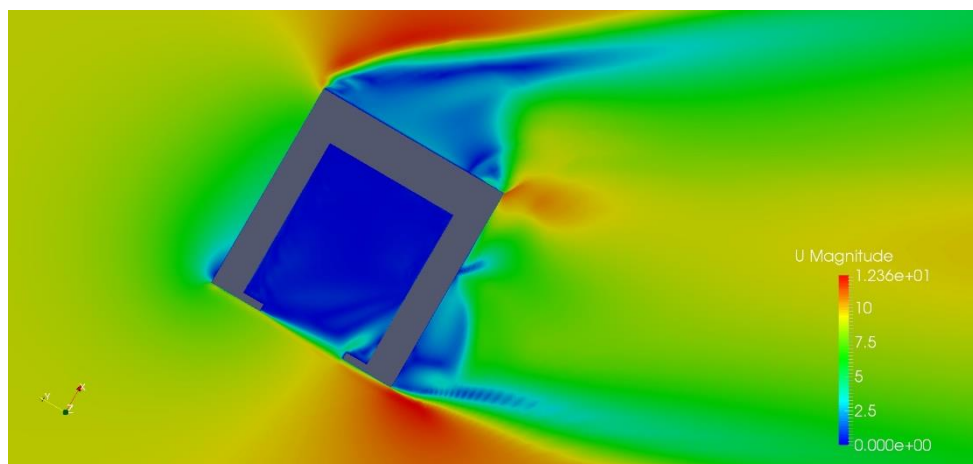


Figure 4-8 Flow field around the cavity ($u = 9 \text{ m/s}$)

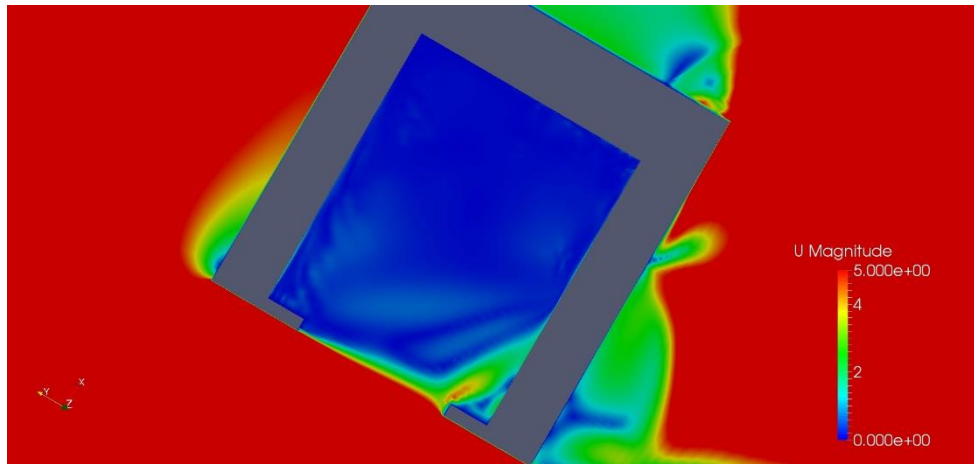


Figure 4-9 Flow field at the aperture ($u = 9 \text{ m/s}$)

As mentioned and can be seen in the Figure 4-10, the stagnation zone is disturbed, and its boundary has moved higher in the cavity and we see a bigger convective zone in the cavity. Also, the temperature in the cavity has generally dropped as the Figure 4-11 shows the temperature values in the cavity.

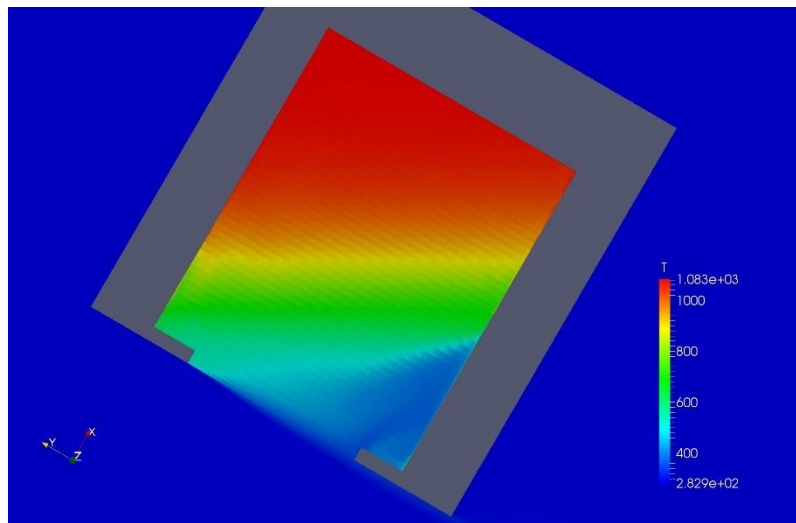


Figure 4-10 Temperature distribution inside cavity ($u = 9 \text{ m/s}$)

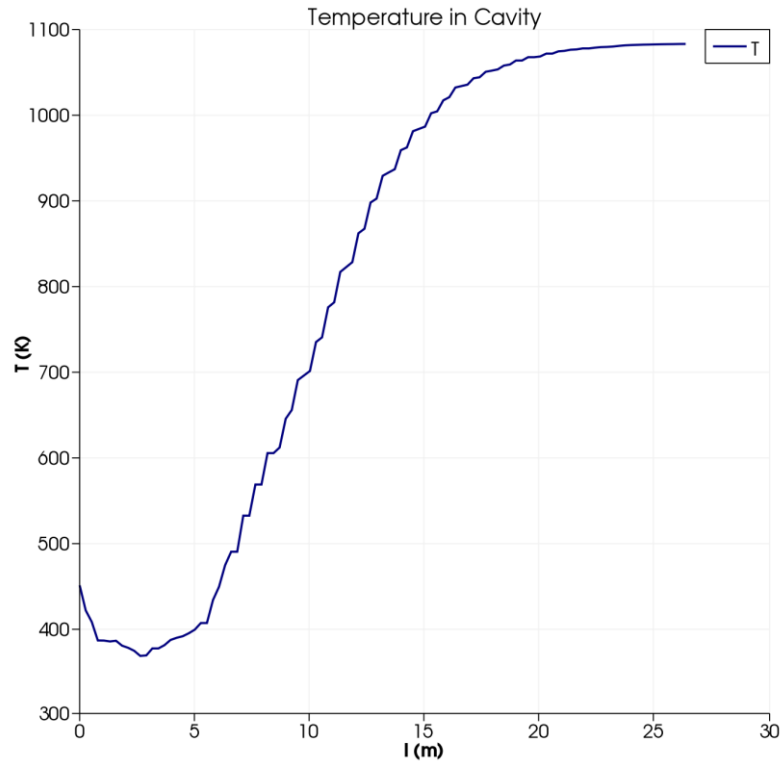


Figure 4-11 Temperature along TRL ($u = 9 \text{ m/s}$)

4.1.3 $u = 15 \text{ m/s}$

As expected, on the higher velocity of $u = 15 \text{ m/s}$, the wind has penetrated more into the cavity and has produced high velocity flows inside the cavity. A shrinkage of the stagnation zone can be seen in the Figure 4-14 as expected and the temperature profile in Figure 4-15 has shifted toward the lower temperature.

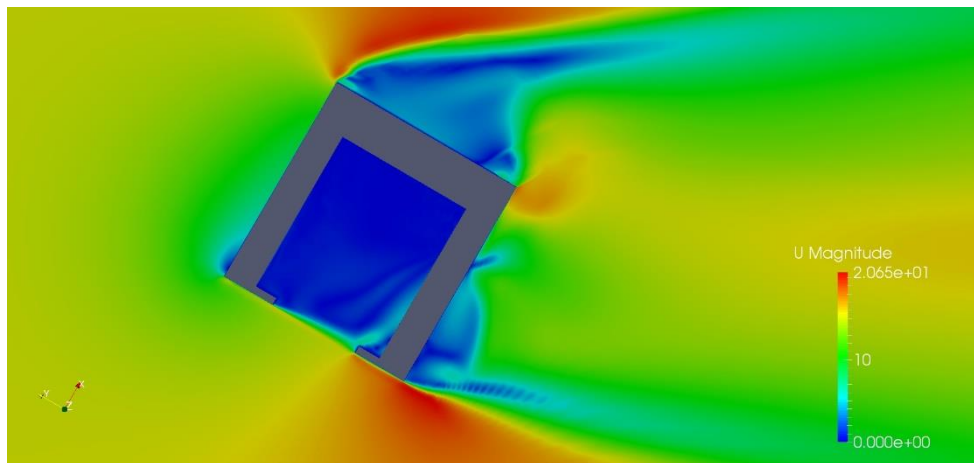


Figure 4-12 Flow field around the cavity ($u = 15 \text{ m/s}$)

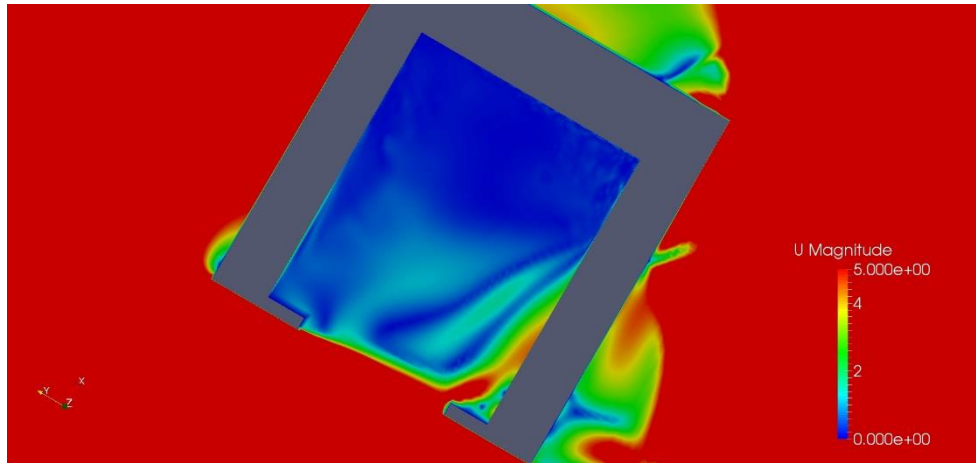


Figure 4-13 Flow field at the aperture ($u = 15 \text{ m/s}$)

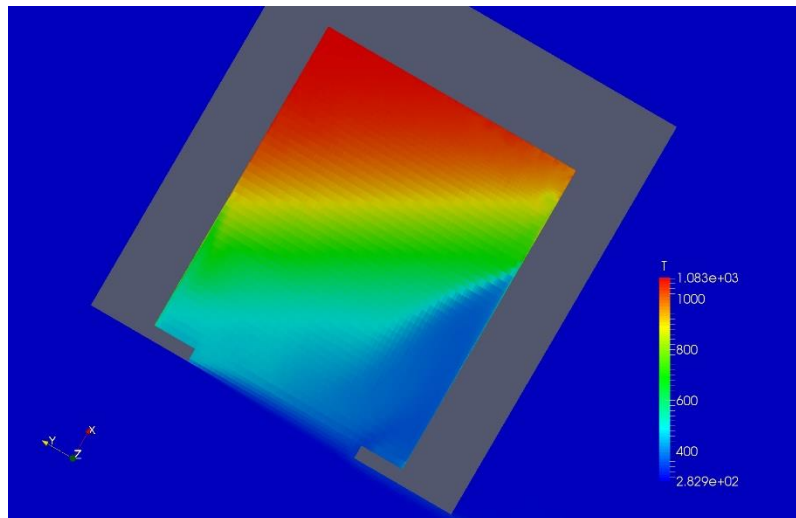


Figure 4-14 Temperature distribution inside cavity ($u = 15 \text{ m/s}$)

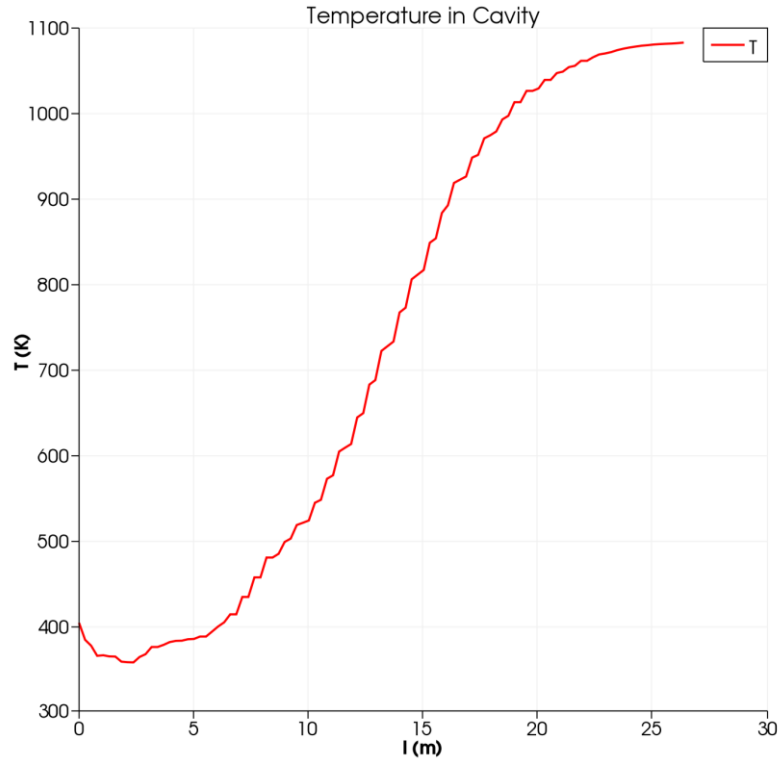


Figure 4-15 Temperature along TRL ($u = 15 \text{ m/s}$)

4.1.4 $u = 19 \text{ m/s}$

This has been the maximum wind velocity that is tested in this study. As we have seen from the trend before, increase of penetration of wind into the cavity and higher velocities inside the cavity is expected. This phenomenon can be seen in the Figure 4-17. The wind has entered to the cavity through the lower parts of the cavity with velocities higher than 5 m/s and it penetrate almost till the middle of the cavity. As we will see, it will definitely have a big impact on the temperature and heat losses inside the cavity.

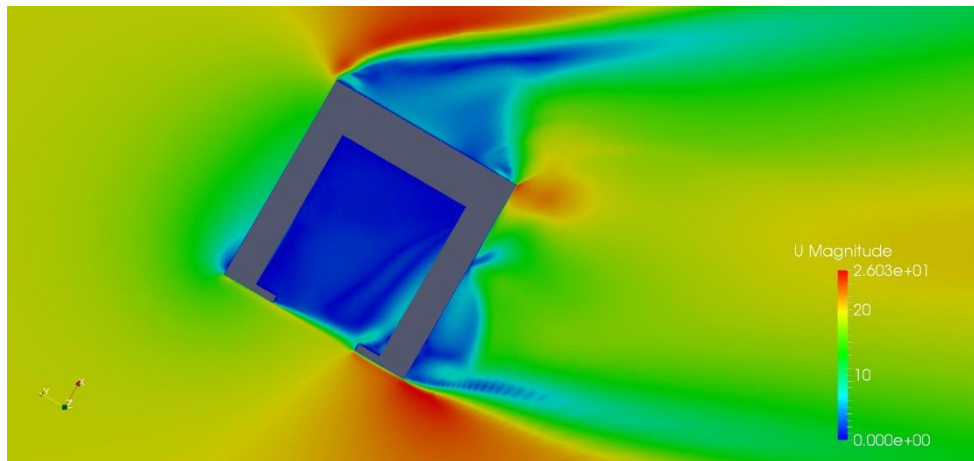


Figure 4-16 Flow field around the cavity ($u = 19 \text{ m/s}$)

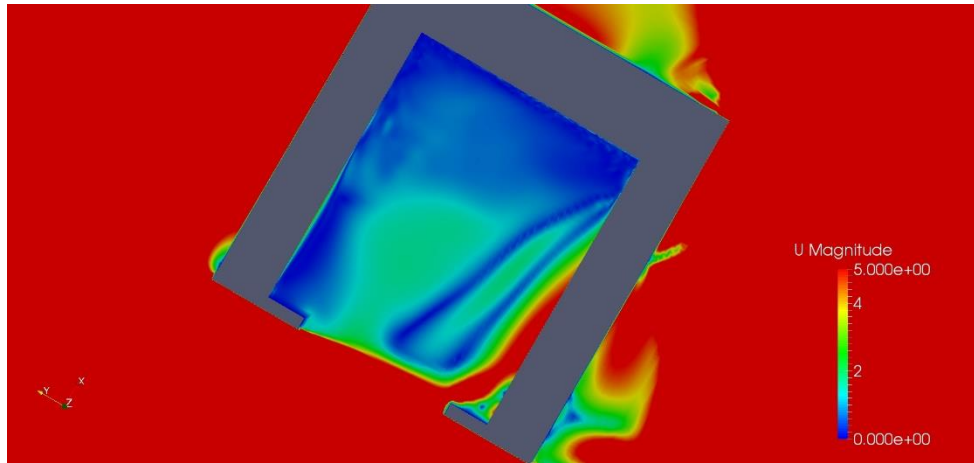


Figure 4-17 Flow field at the aperture ($u = 19$ m/s)

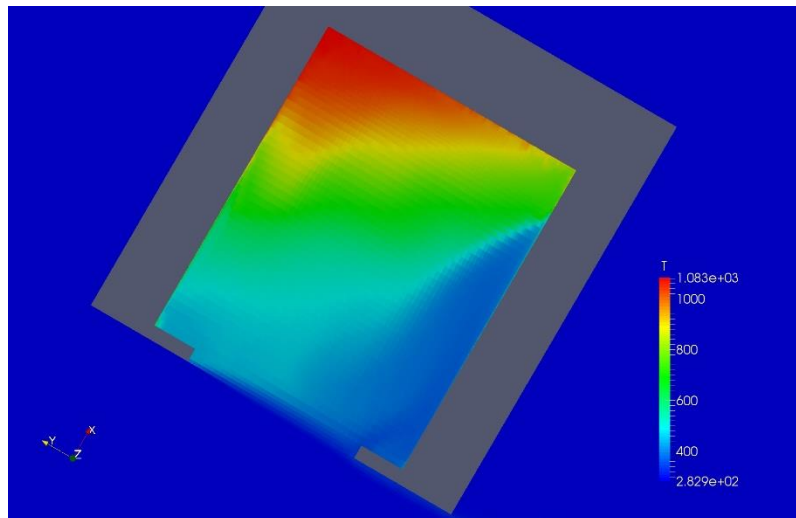


Figure 4-18 Temperature distribution inside cavity ($u = 19$ m/s)

As mentioned before, this level of velocity has opened a channel into the cavity and completely disturbed the stagnation zone. We can hardly see any stagnation zone inside the cavity and the air in the cavity is totally unstable. This can be seen obviously in the temperature diagram inside the cavity as there is no region with maximum temperature of stagnation in the cavity.

All the disturbances and flows inside the cavity will lead to an increase of the heat transfer coefficient on the cavity walls and this will impact the convective heat losses through the internal walls. We will see the heat loss calculations and the comparison of the results in the next section, where the impact of the wind on the convective heat losses will be concluded.

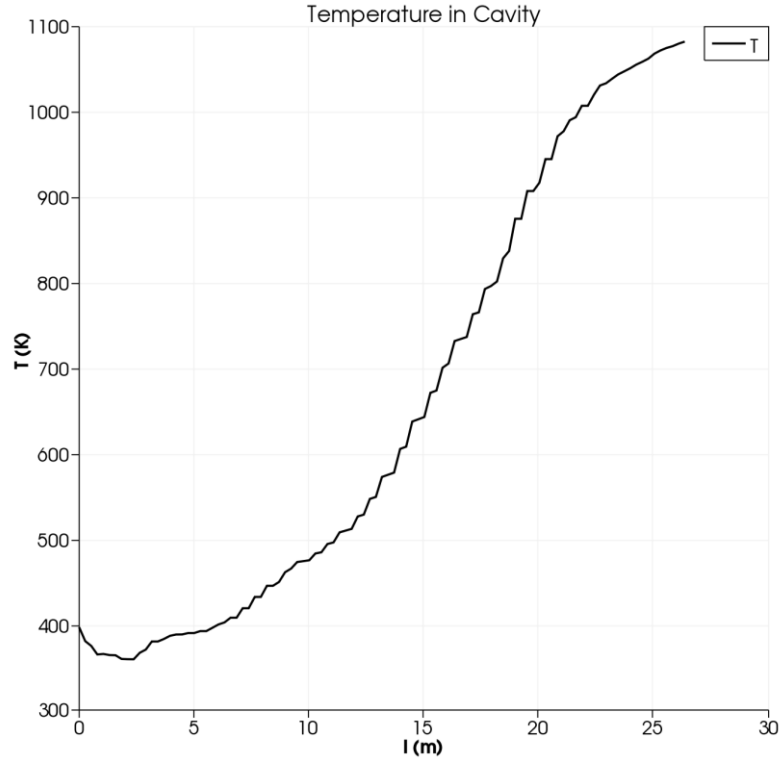


Figure 4-19 Temperature along TRL ($u = 19 \text{ m/s}$)

4.2 Convective Losses from the receiver

In the previous section, the effects of different wind velocities on flow in the cavity, stagnation zone and temperature distribution have been analyzed. In this section, we will compare the results of different cases and evaluate the heat losses from each case to compare them according our observation of each case.

By looking at the Temperature along the TRL line, it is obvious that the increase of wind velocity has reduced the temperature in the cavity and caused shrinkage of the stagnation zone. The overall effect of wind can be seen better by comparing different diagrams and putting them together as it has been done in the Figure 4-20.

According to the comparison in Figure 4-20, wind has a significant effect on the temperature distribution inside the cavity. By considering the cavity as a simple water tube boiler and according to the simple heat transfer equation below, we can understand the importance of ΔT term inside the cavity especially in the stagnation zone.

$$Q = UA\Delta T = UA (T_{st} - T_{water}) \quad (4-4)$$

Where U is the overall heat transfer coefficient, A is the area, T_{st} is the temperature of air in the stagnation zone and T_{water} is the water temperature in the tubes. Higher ΔT in the boiler can lead to a higher Q and a better performance and efficiency of the boiler, using the same heat source.

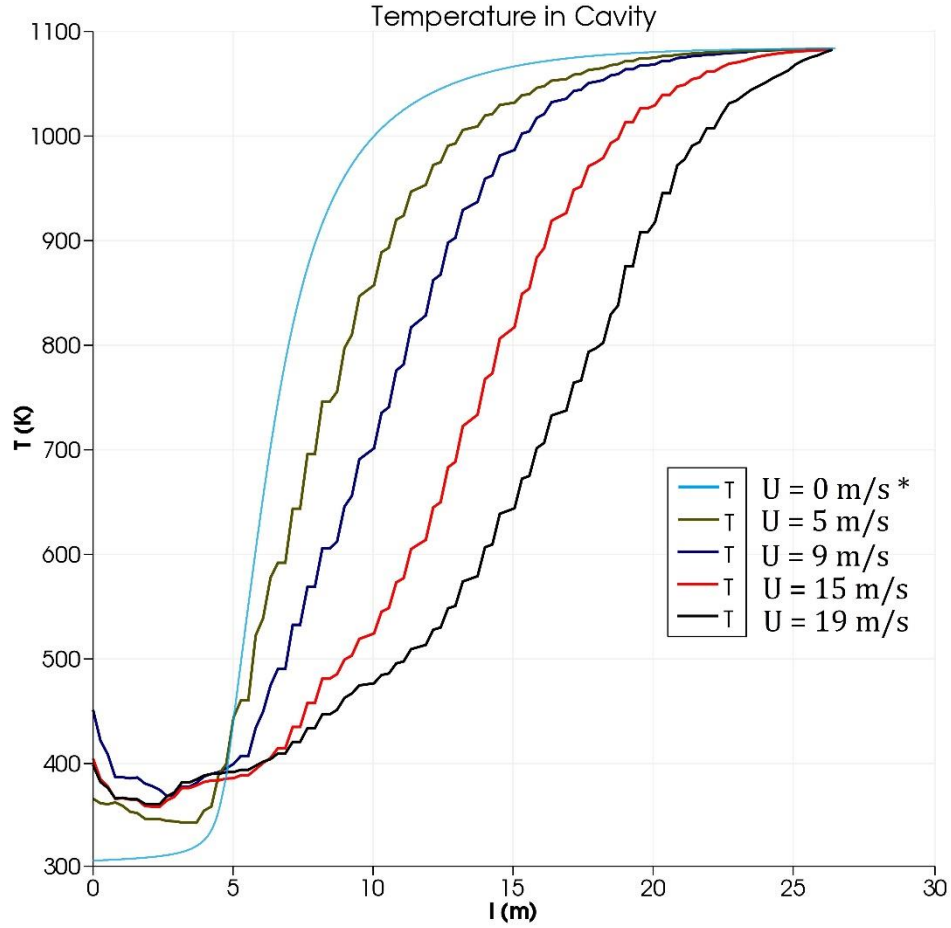


Figure 4-20 Temperature comparison inside cavity with different wind velocities
 * $u = 0 \text{ m/s}$ has not been simulated in the study (diagram is an approximation from literature)

As mentioned in chapter one and two, in this study we have used a uniform constant temperature boundary layer on the internal walls of the cavity only to evaluate and investigate the convective heat losses inside the cavity. To this regard, we can evaluate the convective heat losses of the inner cavity walls using the surface normal gradient of the temperature $\left(\frac{dT}{dn}\right)$ and the local conductivity of the fluid λ by the following formula:

$$\dot{Q}_{conv} = \int_{A_{Cavity}} \lambda, \left(\frac{dT}{dn}\right), dA \quad (4-5)$$

The losses calculated utilizing the Equation ... on the internal walls of the cavity are reported on the Table 4-1.

The dimensionless Nusselt Number will be obtained using the calculated heat losses as follow

$$Nu = \frac{\dot{Q}_{conv,d}}{\Delta T, A_{cavity}, \lambda} \quad (4-6)$$

And the inverse of the Richardson Number as the ratio of the wind influence over the buoyancy influence will be calculate by

$$Ri^{-1} = \frac{Re^2}{Gr} \quad (4-7)$$

$\frac{Re^2}{Gr}$ can be considered as an indicator for the regime of heat transfer in the cavity. A lower ratio shows more importance and effect of the buoyant forces in the cavity and a high value can indicate the important effects of the forced convection in the cavity.

u (m/s)	Q_{conv} (W)	Re	Nu	Re^2/Gr
5	1566896.636	2819940.476	487.070841	4.30E-01
9	2211627.728	5075892.857	687.485921	1.39E+00
15	3486124.141	8459821.429	1083.66396	3.87E+00
19	4487684.988	10715773.81	1394.99981	6.20E+00

Figure 4-21 Convective losses from Cavity

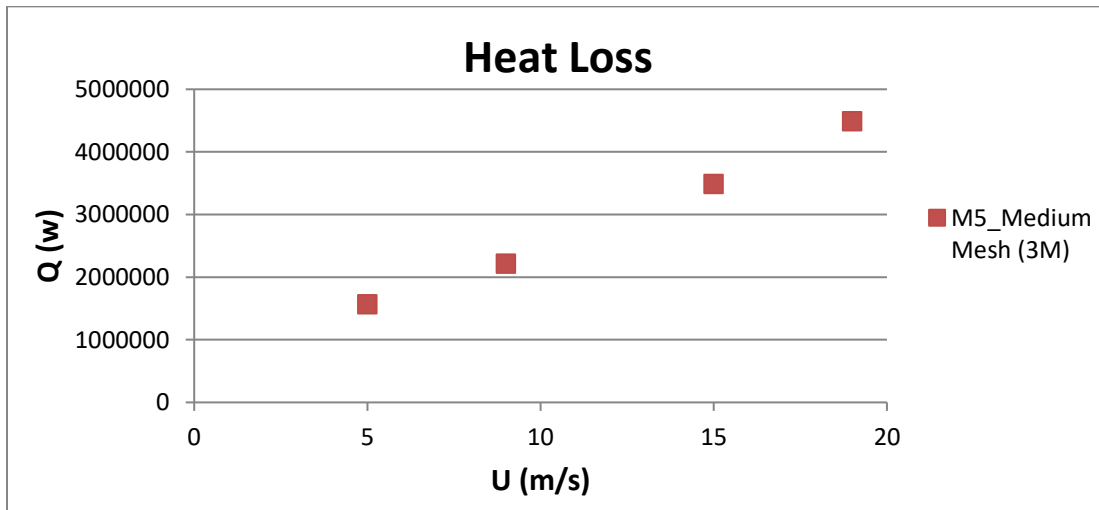


Figure 4-22 Heat losses from cavity walls in all meshes

As we can see from the Figure 4-22 the heat losses inside the cavity are almost increasing linearly with the wind velocity and these heat losses are in a very considerable range.

Shrinkage of the stagnation zone has been observed with all wind velocities and stagnation zone become smaller with higher wind speeds. As the convective heat losses in the stagnation zone are very small, the shrinkage of the stable stagnation zone and consequently a bigger convective zone with lower temperature and natural and convective flows in it,

should be the main reason for the increase of the convective heat losses from the cavity while the wind velocity increases.

Heat losses are reported in the Figure 4-23 on a diagram based on Nusselt Number and the inverse Richardson Number as it has been done in many studies in the literature to compare the convective heat losses in different heat transfer and flow regimes.

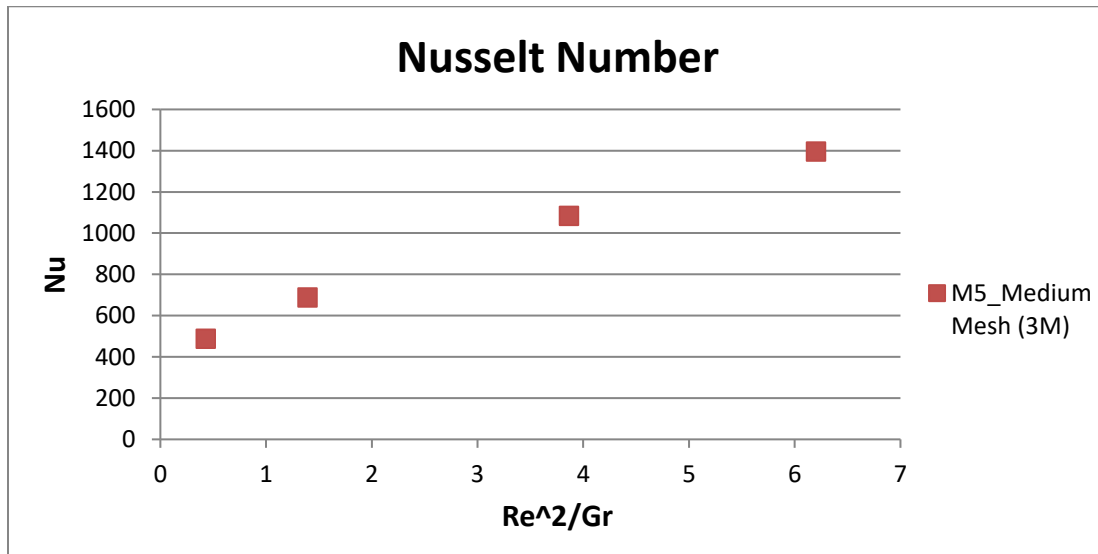


Figure 4-23 Nusselt Number report in different cases

4.3 Influence on the efficiency of the receiver

In this study, the sizing of the cavity is done by assuming a constant heat flux of $200 \frac{kW}{m^2}$ on the internal walls of the cavity and the nominal thermal power related is $75 MW_{th}$.

By considering the $75 MW_{th}$ as the total heat available to the cavity receiver, the percentage of convective heat losses are calculated in Figure 4-24 for all the cases.

u (m/s)	Q_{conv} (kW)	Loss %
5	1566.9	2.09 %
9	2211.6	2.95 %
15	3486.1	4.65 %
19	4487.7	5.98 %

Figure 4-24 Percentage of Convective heat losses

As the percentage of losses is calculated in the Figure 4-24, we can notice that the losses enforced by the convective heat losses for the range of wind speed considered in this study can be in the order of 2 to 6 percent. Obviously, this percentages are calculated assuming the nominal thermal power of 75 MW (by considering the constant heat flux of $200 \frac{kW}{m^2}$ for all the the internal walls of the cavity) and the constant temperature on all the walls in this simulation.

In reality, the heat flux available to the internal walls of the cavity could be less than $200 \frac{kW}{m^2}$, while the temperature of the walls due to the irradiation will remain as high as the value considered in this simulation. Therefore, the nominal power available to the cavity, could be less and possibly in the order of 50 MW. Considering such a value in the efficiency of the cavity receiver with almost the same values of convective losses will result to a cavity heat loss in the range of 4 to 12 percent that is a very considerable value that must be considered and evaluated in the design and operation of the solar power towers.

4.4 Convergence and Mesh sensitivity analysis

As mentioned in chapter 3, in this study three different meshes have been used. Due to the fact that wall functions have been used for the turbulence modelling, the first elements on the boundary layer had to meet the minimum requirements of the wall functions but in the rest of the geometry, varied sizes of elements have been used and the three different meshes with almost 1, 3 and 10 million elements have been used. According to the objective of this study, the heat losses through the internal walls of the cavity have been tracked and used as the convergence criteria.

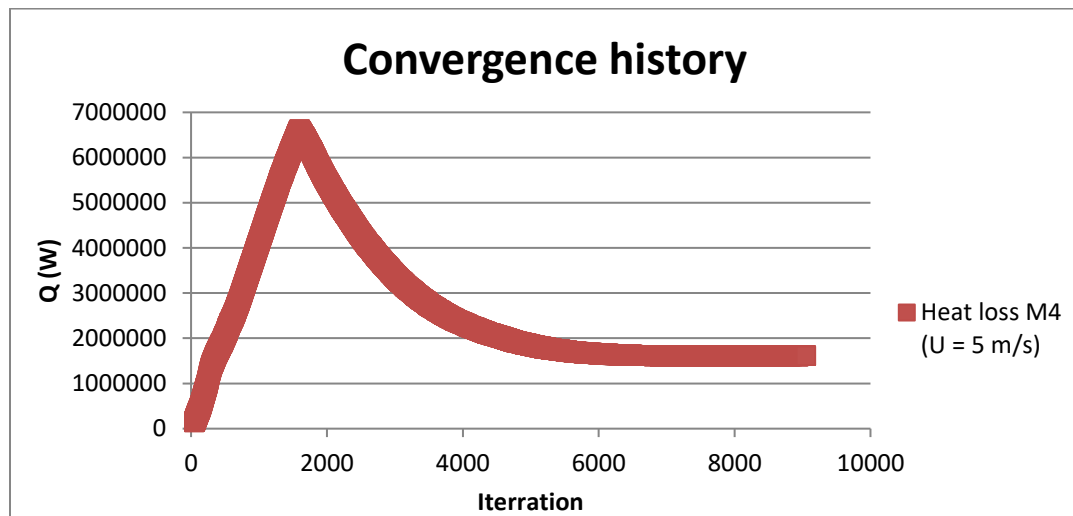


Figure 4-25 Convergence history M4 (u = 5 m/s)

The results of this analysis and the convergence history of the simulations are presented in the figures 4-25, 4-26 and 4-27. All the cases have been checked for the convergence and only the convergence history of the M4 Mesh for the velocity of 5 m/s has been reported as an example.

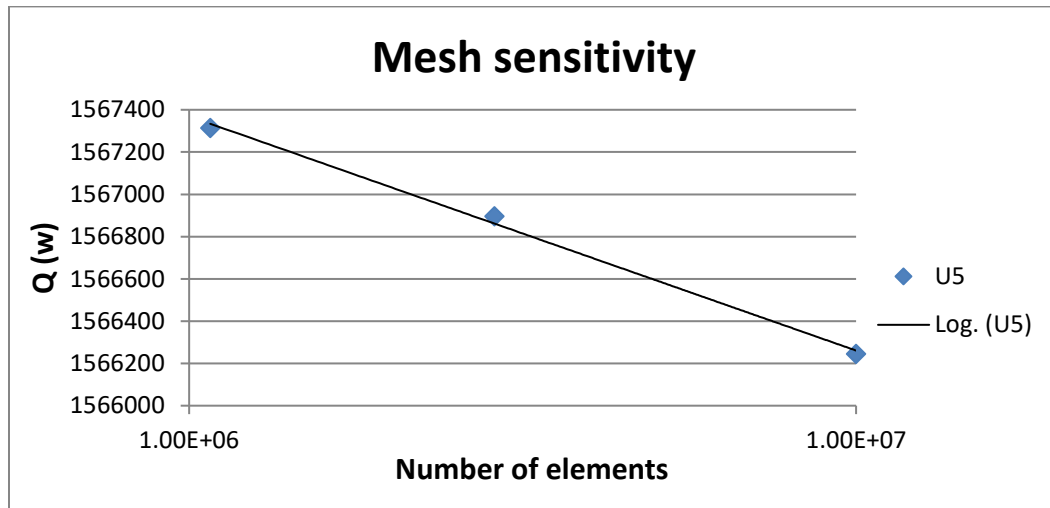


Figure 4-26 Mesh sensitivity on u = 5 m/s

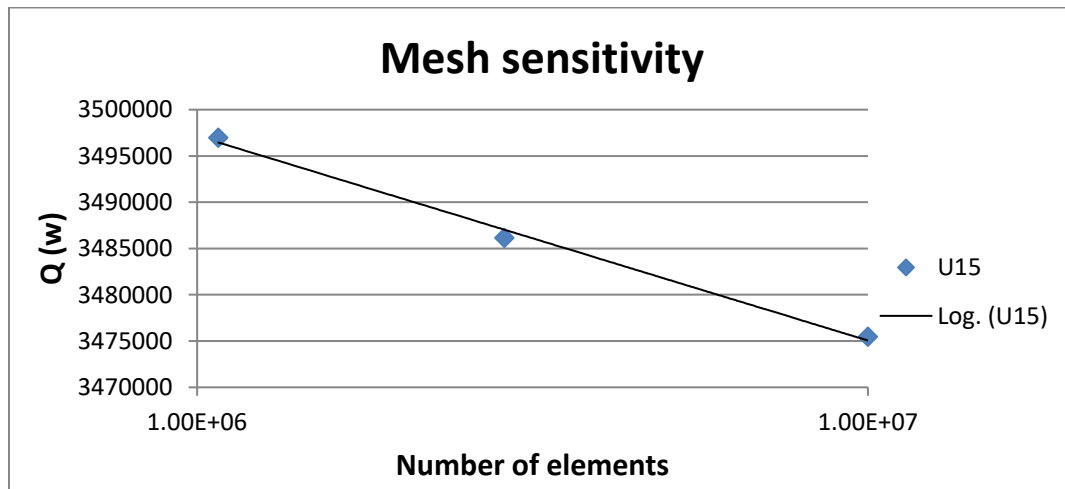


Figure 4-27 Mesh sensitivity on u = 15 m/s

The Mesh sensitivity diagrams have been reported on a logarithmic scale here and the linear line between them indicates the good convergence of the mesh sensitivity analysis.

5 CONCLUSION AND OUTLOOK

In the present study, the effects of wind with Reynolds numbers in the range of $Re = 2.82 \times 10^6 - 1.07 \times 10^7$ on a cavity receiver with inclination of $\phi = 60^\circ$ and a Grashof Number of $Gr = 1.85 \times 10^{13}$ has been investigated and analyzed numerically. The results of this simulation can lead to a better prediction of thermal losses from the cavity receiver of solar thermal towers as a renewable source of energy with multiple applications.

The full set of equations in this work, the continuity equation, Navier–Stokes equation and energy equation were solved using the CFD code in OpenFOAM 2.3.0. As the meshing tool of OpenFOAM is not very capable in the meshing of complex geometries, ANSYS ICEM CFD 16.2 has been used for meshing and the output has been translated into OpenFOAM format for the simulations. In the post-processing phase, ParaView has been used as the main post-processing tool provided with OpenFOAM.

Many studies in the literature have tried to investigate the convective heat losses from the cavity receivers and some of them have considered the wind effects in their studies. Most of these studies have concluded an increase on the convective heat losses in the presence of wind, which is in contrast with predictions of Clausius model. However, the level of increase in convective heat losses are not accordant to each other and general conclusion in most of studies shows that this kind of increase can be highly geometry and case dependent.

This study has tried to investigate convective heat losses from a real scale cavity receiver with the nominal thermal power of $75 MW_{th}$. As of now, this project is one of the first real scale simulations that has been carried out on cavity receivers with the $Gr > 10^{13}$. This level of Grashof number, dimension and temperature was not investigated in the previous researches. Results of this study shows that the convective heat losses in this scale and inclination level is highly related to forced convection induced by wind and can significantly affects the efficiency of the receiver. The results show an almost linear relation between the

convective heat losses and wind velocity. This means that effective reduction strategies have to be implemented in the design of the cavity receivers for industrial and commercial usages.

The simulations on this study have been carried out for a single geometry, 60-degree inclination of cavity and head-on wind. Other geometries, inclinations and side winds should be investigated for a more comprehensive result. Also, a more realistic thermal boundary condition has to be defined along with the radiation simulations in the future studies for a more practical simulation and comprehensive results.

Validation of such numerical simulations, require experimental data and factual information from already built solar towers with the cavity technology, but as of now the best comparison can be done by considering the mathematical models and the dimensionless models obtained from the small scale experimental studies and the validated numerical simulations.

LITERATURE

[1] R.K. McMordie. Convection heat-loss from a cavity receiver. *J. Solar Energy Eng.-Trans. ASME* 106, 98 – 100, (1984).

[2] R. Uhlig, R. Flesch. “Strategies Enhancing Efficiency of Cavity Receivers”. In: *Energy Procedia* 49, S. 538–550, (2014).

[3] J. Kraabel. An experimental investigation of the natural convection from a side-facing cubical cavity. In: Mori Y, Yang WJ., (Eds.), American Society of Mechanical Engineers, Japan Society of Mechanical Engineers, Proceedings of the ASME–JSME Thermal Engineering Joint Conference, vol. 1, pp. 299 – 306, (1983).

[4] L.L. Eyster. Predictions of Convective Losses from a Solar Cavity Receiver. Technical Report, Battelle Pacific Northwest Labs, Richland, WA (USA). (1979).

[5] A.M. Clausing. An analysis of convective losses from cavity solar central receivers, *Sol. Energy* 27. 295 – 300, (1981).

[7] J.B. Fang, J.J. Wei, X.W. Dong, Y.S. Wang, Thermal performance simulation of a solar cavity receiver under windy conditions, *Sol. Energy* 85. 126 – 138, (2011).

[8] T. Tan, Y. Chen, Z. Chen, N. Siegel, G.J. Kolb, Wind effect on the performance of solid particle solar receivers with and without the protection of an aero window, *Sol. Energy* 83. 1815 – 1827, (2009).

[9] P. Liovic, J.-S. Kim, G. Hart, W. Stein, Wind dependence of energy losses from a solar gas reformer, *Appl. Therm. Eng.* 63. 333 – 346, (2014).

[10] R. Flesch, H. Stadler, R. Uhlig, B. Hoffschmidt, On the influence of wind on cavity receivers for solar power towers: An experimental analysis, *Applied Thermal Engineering* 87. 724 – 735, (2015).

- [11] Ma, R. Y. Wind Effect on Convective Heat Loss from a Cavity Receiver for a Parabolic Concentrating Solar Collector. Sandia National Laboratories, (1993).
- [12] Flesch, R., Stadler, H. u. a. „Numerical Analysis of the Influence of Inclination Angle and Wind on the Heat Losses of Cavity Receivers for Solar Thermal Power Towers “. In: Solar Energy 110. 427 – 437, (2014).
- [13] W. Stine, C. McDonald, Cavity receiver heat loss measurements, ISES World Congress, (1989).
- [14] T. Taumoefolau, S. Paitoonsurikarn, G. Hughes, K. Lovegrove, Experimental investigation of natural convection heat loss from a model solar concentrator cavity receiver, J. Sol. Energy Engin. Trans. ASME 126. 801 – 807, (2004).
- [15] S. Paitoonsurikarn, K. Lovegrove, G. Hughes, J. Pye, Numerical investigation of natural convection loss from cavity receivers in solar dish applications, J. Sol. Energy Eng. Trans. ASME 133. 10, (2011).
- [16] S.Y. Wu, L. Xiao, Y.R. Li, Effect of aperture position and size on natural convection heat loss of a solar heat-pipe receiver, Appl. Therm. Eng. 31. 2787 – 2796, (2011).
- [17] W. Wu, L. Amsbeck, R. Buck, N. Waibel, P. Langner, R. Pitz-Paal, On the influence of rotation on thermal convection in a rotating cavity for solar receiver applications, Appl. Therm. Eng. 70. 694 – 704, (2014).
- [18] S. Paitoonsurikarn, T. Taumoefolau, K. Lovegrove, Estimation of convection loss from paraboloidal dish cavity receivers, in: Proceedings of 42nd Conference of the Australia and New Zealand Solar Energy Society (ANZSES), (2004).
- [19] L. Xiao, S.-Y. Wu, Y.-R. Li, Numerical study on combined free-forced convection heat loss of solar cavity receiver under wind environments, Int. J. Therm. Sci. 60. 182 – 194, (2012).
- [20] M. Prakash, S.B. Kedare, J.K. Nayak, Investigations on heat losses from a solar cavity receiver. Sol. Energy 83. 157 – 170, (2009).
- [21] S.-Y. Wu, F.-H. Guo, L. Xiao, Numerical investigation on combined natural convection and radiation heat losses in one side open cylindrical cavity with constant heat flux, Int. J. Heat Mass Transf. 71: 573 – 584, (2014).
- [22] S.-Y. Wu, Z.-G. Shen, L. Xiao, D.-L. Li, Experimental study on combined convective heat loss of a fully open cylindrical cavity under wind conditions, Int. J. Heat Mass Transf. 83. 509 – 521, (2015).
- [23] D.C. Wilcox. Turbulence Modeling for CFD. DCW Industries, Incorporated, (1994).
- [24] Introduction to Simulation. <http://www.cats.rwth-aachen.de/library/research/simulation>.
- [25] D.C. Wilcox. Turbulence Modeling for CFD. DCW Industries, Incorporated, (1994)

[26] P. Srinivasa Rao. Modeling of Turbulent Flows and Boundary Layer, Computational Fluid Dynamics. (2010).

[27] Tsan-Hsing Shih, William W. Liou, Aamir Shabbir, Zhigang Yang, and Jiang Zhu. A new k-epsilon eddy viscosity model for high reynolds number turbulent flows. Computers and Fluids, 24(3): 227 – 238, (1994).

[28] Md. Rahman, Md. Karim, and Md. Alim. Numerical investigation of unsteady flow past a circular cylinder using 2-d finite volume method. Journal of Naval Architecture and Marine Engineering, 4(1), (2008).

[29] K. An, J.C.H. Fung, and S.H.L. Yim. Sensitivity of inflow boundary conditions on downstream wind and turbulence profiles through building obstacles using a CFD approach. Journal of Wind Engineering and Industrial Aerodynamics, 115(0):137 – 149, (2013).

[30] F. R. Menter. Zonal Two-equation k- ϵ Turbulence Models for Aerodynamic Flows. AIAA, 01(26):641 – 648, (1994).

[31] F. R. Menter. Two-equation Eddy Viscosity Turbulence Models for Engineering Applications. AIAA, 32(8):1598 – 1605, (1994).

[32] Wall Functions and y^+ requirements.
<http://www.computationalfluidynamics.com.au/tips-tricks-turbulence-wall-functions-and-y-requirements/>.

[33] Z. Mahdi. Numerical Investigation of Constructive Measures to Reduce Convective Losses of Solar Thermal Power Plants. Aachen University of Applied Sciences, (2014).

[34] J. Grobbel. Development and Numerical Investigation of Reduction Strategies for Convective Heat Losses of Cavity Receivers Used in Solar Thermal Power Towers. RWTH Aachen University, (2014).

[35] OpenFOAM user manual. <http://www.openfoam.com>.

[36] ANSYS ICEM CFD user manual. <http://www.ansys.com/en-in/products/fluids>.

[37] LM. Murphy. Wind loading on tracking and field mounted solar collectors. Technical Report for Colorado State University. Report No. SERI/TP. 632 – 958, (1980)